



HAL
open science

Linear stability and sensitivity of the flow past a fixed oblate spheroidal bubble

Joël Tchoufag, Jacques Magnaudet, David Fabre

► **To cite this version:**

Joël Tchoufag, Jacques Magnaudet, David Fabre. Linear stability and sensitivity of the flow past a fixed oblate spheroidal bubble. *Physics of Fluids*, 2013, vol. 25, 10.1063/1.4804552 . hal-00874779

HAL Id: hal-00874779

<https://hal.science/hal-00874779>

Submitted on 18 Oct 2013

HAL is a multi-disciplinary open access archive for the deposit and dissemination of scientific research documents, whether they are published or not. The documents may come from teaching and research institutions in France or abroad, or from public or private research centers.

L'archive ouverte pluridisciplinaire **HAL**, est destinée au dépôt et à la diffusion de documents scientifiques de niveau recherche, publiés ou non, émanant des établissements d'enseignement et de recherche français ou étrangers, des laboratoires publics ou privés.



Open Archive TOULOUSE Archive Ouverte (OATAO)

OATAO is an open access repository that collects the work of Toulouse researchers and makes it freely available over the web where possible.

This is an author-deposited version published in : <http://oatao.univ-toulouse.fr/>
Eprints ID : 9792

To link to this article :DOI :10. 1063/1.4804552
URL : <http://dx.doi.org/10.1063/1.4804552>

To cite this version : Tchoufag, Joel and Magnaudet, Jacques and Fabre, David *Linear stability and sensitivity of the flow past a fixed oblate spheroidal bubble*. (2013) *Physics of Fluids*, vol. 25 (n° 054108). ISSN 1070-6631

Any correspondence concerning this service should be sent to the repository administrator: staff-oatao@listes-diff.inp-toulouse.fr

Linear stability and sensitivity of the flow past a fixed oblate spheroidal bubble

J. Tchoufag,¹ J. Magnaudet,^{1,2} and D. Fabre¹

¹*Université de Toulouse, INPT, UPS, IMFT (Institut de Mécanique des Fluides de Toulouse), Allée Camille Soula, 31400 Toulouse, France*

²*CNRS, IMFT, 31400 Toulouse, France*

The stability properties of the wake past an oblate spheroidal bubble held fixed in a uniform stream are studied in the framework of a global linear analysis. In line with previous studies, provided the geometric aspect ratio of the bubble, χ , is large enough, the wake is found to be unstable only within a finite range of Reynolds number, Re . The neutral curves corresponding to the occurrence of the first two unstable modes are determined over a wide range of the (χ, Re) domain and the structure of the modes encountered along the two branches of each neutral curve is discussed. Then, using an adjoint-based approach, a series of sensitivity analyses of the flow past the bubble is carried out in the spirit of recent studies devoted to two-dimensional and axisymmetric rigid bodies. The regions of the flow most sensitive to an external forcing are found to be concentrated in the core or at the periphery of the standing eddy, as already observed with bluff bodies at the surface of which the flow obeys a no-slip condition. However, since the shear-free condition allows the fluid to slip along the bubble surface, the rear half of this surface turns out to be also significantly sensitive to disturbances originating in the shear stress, a finding which may be related to the well-known influence of surfactants on the structure and stability properties of the flow past bubbles rising in water.

I. INTRODUCTION

The dynamics of isolated bubbles rising in a fluid otherwise at rest has attracted attention for ages, especially in the regime where bubble paths exhibit oscillations.¹ Path instability gave rise to many speculations,² until the role of the wake was made clear during the last 15 years through the combined design and use of refined experiments³⁻⁶ and computations;⁷⁻¹⁰ a recent review of the corresponding state-of-the-art may be found in Ref. 11. Influence of contamination by surfactants on this instability also starts to be understood and quantified.¹²

Despite these progresses, many aspects of the problem still require clarification. In particular, establishing properly the connections and structural differences between the dynamics of the coupled bubble-fluid problem where the bubble is free to rise and those of the wake past a bubble artificially forced to set fixed in a uniform stream is an important step. Indeed, recent theoretical and computational studies devoted to two- and three-dimensional rigid bodies such as ellipses,¹³ plates,¹⁴ or disks¹⁵ revealed that, although the presence of vorticity in the flow is at the root of path instability, there may be little connection between the fixed-body and freely moving-body problems: the thresholds and frequencies may be totally different, as can be the wake structure and the dynamics of the shedding process. Direct numerical simulation (DNS) based on the full Navier-Stokes equations obviously provides a complete picture of the flow field and how it is affected by allowing or suppressing the kinematic degrees of freedom of the body. Nevertheless it does not give a direct access to the individual growth rate and spatial structure of the first unstable modes, nor does it provide insight into the way their properties may be modified by slightly changing some characteristics of the base flow. Linear stability analysis (LSA) appears to be the most appropriate approach

to address such questions. Moreover, owing to limitations in the computational resources, the only LSA of the flow past a fixed bubble available to date¹⁰ had a limited accuracy and did not explore a wide range of control parameters. For these various reasons, revisiting the LSA problem for the flow past a fixed spheroidal bubble is in order.

A recent stream of research making systematic use of linearized techniques based on adjoint methods has developed in connection with problems of passive control of separated flows past bluff bodies (see Ref. 16 for a review). Applying this approach to the flow past a bubble may shed some light on the similarities and differences resulting from the presence of a shear-free condition at the bubble surface, as opposed to the no-slip condition involved in all available studies, most of which focused on two-dimensional circular cylinders^{17–20} and axisymmetric rigid bodies such as spheres, disks,^{21,22} or bullet-shaped bodies.^{23,24}

In the first part of the paper, we revisit the linear stability of the wake past a spheroidal bubble with a prescribed shape held fixed in a uniform stream. After summarizing the computational approach and the solution procedure in Secs. II and III, respectively, we describe in Sec. IV the structure of the global modes and their stability properties as a function of the two control parameters of the problem, namely, the bubble geometric aspect ratio, χ , and the flow Reynolds number, Re . We systematically explore the region $\chi \leq 2.7$, $Re \leq 3500$, thus covering a much broader range than the previous LSA of the same problem.¹⁰

In Sec. V we compute the adjoint of the base flow and of the global modes to explore effects of external disturbances on wake instability. These effects are evaluated via a series of sensitivity analyses based on either a local forcing of the flow or on a systematic computation of the variations of the eigenvalues to changes in the properties of the base flow. The formulation we use allows us to study effects of changes in the bulk (i.e., in the velocity field) as well as in the normal velocity and shear stress possibly acting right at the bubble surface. The focus put on the latter aspect may help understand how surfactants which are known to change the boundary condition at the surface of drops and bubbles moving in polar liquids (especially water) influence the stability properties of the corresponding wakes.

II. PROBLEM CONFIGURATION AND NUMERICAL APPROACH

The inescapable importance of the wake in the process leading to path instability of a freely rising bubble^{4,9} is assessed by suppressing the bubble translational and rotational degrees of freedom and prescribing its shape. Since small bubbles rising along a zigzag path are known to approach an oblate spheroidal shape with only minor variations along the path (this is typically the case for millimetric-sized bubbles rising in water³), we adopt this simplified shape as a leading-order approximation throughout this study. Given the range of Reynolds number we wish to explore, this assumption is only valid as far as surface tension effects may compete with inertial effects, i.e., the Weber number is of order unity.

The simplified configuration under consideration is depicted in Figure 1. In what follows, we only consider moderately oblate bubbles with aspect ratios χ in the range $[1.5, 2.7]$, where $\chi = b/a$ is defined as the ratio between the major and minor semi-axes of the spheroid. In addition to χ , the

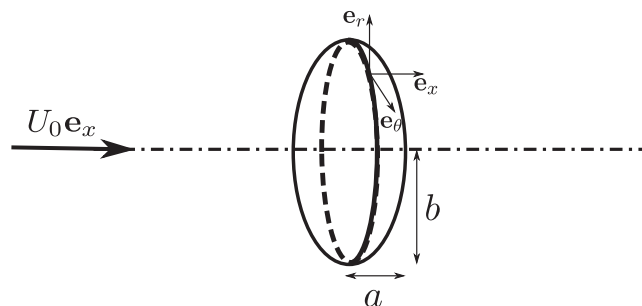


FIG. 1. Problem configuration. The minor axis of the bubble is parallel to the flow at infinity.

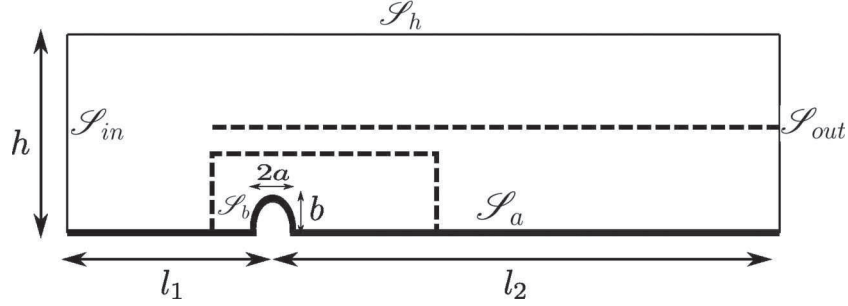


FIG. 2. Sketch of the computational domain \mathcal{D} .

problem depends on the Reynolds number $Re = U_0 d / \nu$, where d is the bubble equivalent diameter ($d = 2(b^2 a)^{1/3}$), U_0 is the velocity at infinity and ν denotes the fluid kinematic viscosity.

The flow is governed by the incompressible Navier-Stokes equations which, when written in dimensionless form read

$$\partial_t \mathbf{U} + \mathbf{U} \cdot \nabla \mathbf{U} = -\nabla P + Re^{-1} \nabla^2 \mathbf{U}, \quad (1a)$$

$$\nabla \cdot \mathbf{U} = 0, \quad (1b)$$

$$\mathbf{n} \times (\nabla \mathbf{U} + \nabla \mathbf{U}^T) \cdot \mathbf{n} = \mathbf{0} \text{ on } \mathcal{S}_b, \quad (1c)$$

$$\mathbf{U} \cdot \mathbf{n} = 0 \text{ on } \mathcal{S}_b, \quad (1d)$$

$$\mathbf{U} \rightarrow \mathbf{e}_x \text{ for } \|\mathbf{x}\| \rightarrow \infty, \quad (1e)$$

where \mathcal{S}_b stands for the bubble surface, \mathbf{n} is the local unit normal, \mathbf{x} is the local distance to the bubble center, and \mathbf{e}_x is the unit vector in the streamwise direction, i.e., collinear to the velocity at infinity. Equations (1c) and (1d) express the shear-free and no-penetration conditions at the bubble surface, respectively; while Eq. (1e) expresses the vanishing of the velocity disturbance at infinity.

The FreeFem++ software based on a finite element method is used to solve the problem numerically. The computational domain \mathcal{D} sketched in Figure 2 is discretized via a Delaunay-Voronoi algorithm which generates triangular elements. The dashed lines shown in Figure 2 indicate the zones where a local refinement is applied because it is anticipated that crucial aspects of the dynamics take place in the vicinity of the bubble and in its wake. The far-field condition (1e) is imposed at the inlet of the domain, while a zero-traction condition is imposed at the outlet. The boundary conditions on the lateral surface \mathcal{S}_h and symmetry axis \mathcal{S}_a of the domain will be specified later. In all cases, these conditions allow us to restrict the discretization the corresponding problem to a half-domain, as depicted in Figure 2.

In order to perform a LSA of the problem, the flow is classically decomposed into a steady base flow plus a small perturbation in the form $\mathbf{U} = \mathbf{U}_0 + \epsilon \mathbf{u}$, $P = P_0 + \epsilon p$. Introducing this ansatz into Eqs. (1a)–(1e) yields a zeroth-order nonlinear problem and a first-order linear problem, both of which involve matrices easily constructed with FreeFem++. At each order of the problem, a variational formulation of the system (1) is built using $P2$ elements for each component of the velocity and $P1$ elements for the pressure and the normal stress $\Sigma = \mathbf{n} \cdot (\nabla \mathbf{U} + \nabla \mathbf{U}^T) \cdot \mathbf{n}$ on \mathcal{S}_b which, in problems involving a free-slip surface, has to be computed as an additional unknown²⁵ to satisfy properly the condition (1c). Details about this variational formulation and the way Σ gets involved in it are provided in Appendix A. After a classical Galerkin projection, the “stiffness” and “mass” matrices are straightforwardly built in FreeFem++ thanks to the embedded UMFPAK library, while the SLEPc library is used to compute the generalized eigenpairs of the corresponding linear stability problem. Influence of the lateral confinement (h), position of the inlet (l_1) and outlet (l_2) boundaries and of the grid density (N) on the drag coefficient of the base flow and first two

eigenvalues of the problem slightly beyond the corresponding threshold is displayed in Table II of Appendix B.

III. SOLUTION PROCEDURE

A. Base flow

The governing equations of the base flow merely correspond to the steady version ($\partial_t(\cdot) = 0$) of the set of Eqs. (1), namely,

$$\mathbf{U}_0 \cdot \nabla \mathbf{U}_0 = -\nabla P_0 + Re^{-1} \nabla^2 \mathbf{U}_0, \quad (2a)$$

$$\nabla \cdot \mathbf{U}_0 = 0, \quad (2b)$$

$$Re^{-1}(\nabla \mathbf{U}_0 + \nabla \mathbf{U}_0^T) \cdot \mathbf{n} = (\Sigma_0 + P_0)\mathbf{n} \text{ on } \mathcal{S}_b, \quad (2c)$$

$$\mathbf{U}_0 \cdot \mathbf{n} = 0 \text{ on } \mathcal{S}_b, \quad (2d)$$

$$\mathbf{U}_0 = \mathbf{e}_x \text{ on } \mathcal{S}_{in}, \quad (2e)$$

$$\mathbf{e}_r \cdot \mathbf{U}_0 = (\mathbf{e}_r \cdot \nabla)(\mathbf{U}_0 \cdot \mathbf{e}_x) = 0 \text{ on } \mathcal{S}_h \cup \mathcal{S}_a, \quad (2f)$$

$$-P_0 \mathbf{n} + Re^{-1}(\nabla \mathbf{U}_0 + \nabla \mathbf{U}_0^T) \cdot \mathbf{n} = \mathbf{0} \text{ on } \mathcal{S}_{out}, \quad (2g)$$

where Σ_0 denotes the base normal stress at the bubble surface and \mathbf{e}_r stands for the unit vector in the radial direction (in what follows $r = \mathbf{x} \cdot \mathbf{e}_r$ and $x = \mathbf{x} \cdot \mathbf{e}_x$ denote the streamwise and radial coordinates, respectively). Equation (2f) expresses the fact that \mathcal{S}_a is a symmetry axis for the base flow and that \mathcal{S}_h is assumed to be a streamline of that flow where it obeys a shear-free condition. The problem (2) being nonlinear, its solution is approached using an iterative Newton method as in Ref. 18. Figure 3 shows a cross-section of the streamlines and isovalues of the streamwise velocity around a bubble with $\chi = 2.5$. At $Re = 155$ (Figure 3(a)), the length of the standing eddy behind the bubble is about $1.63d$; the separation line along the bubble surface stands at $z = 0.16$, $r = 0.56$. This standing eddy is known to exist only when a sufficient amount of vorticity accumulates around the bubble.²⁶ This is why it is observed only for bubbles with a sufficient oblateness ($\chi \geq 1.65$ according to Ref. 27) and within a finite range of Re . The latter trend may be inferred from (Figure 3(b)) corresponding to $Re = 2000$: the length of the standing eddy is then reduced to $0.3d$, indicating that it is gradually shrinking as Re goes on increasing. By increasing further the Reynolds number, we found that it eventually vanishes at $Re \approx 3095$ for that particular aspect ratio.

We checked the accuracy of these results by comparing the drag on the bubble with predictions provided in previous studies^{27,28} throughout the range $10^2 \leq Re \leq 10^3$. This comparison is reported in Table I. A very good overall agreement is observed, regardless of the aspect ratio and Reynolds number.

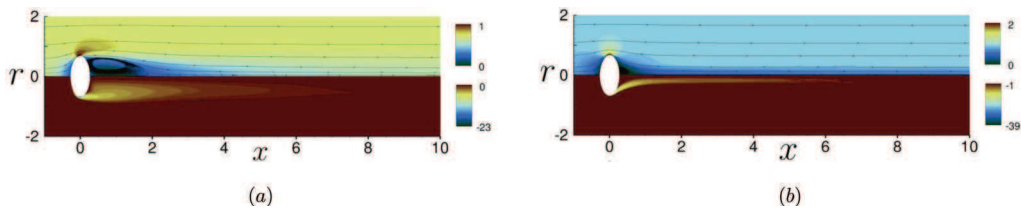


FIG. 3. Base flow around a bubble with $\chi = 2.5$: (a) $Re = 155$; (b) $Re = 2000$. Top half: axial velocity and streamlines; bottom half: azimuthal vorticity.

TABLE I. Drag coefficient C_D for a steady axisymmetric flow past the bubble in the range $10^2 \leq Re \leq 10^3$. Comparison between present study, results from DNS reported in Ref. 27 (only bubbles with $\chi \leq 1.95$ were considered in that study), and predictions from an approximate correlation proposed in Ref. 28. The drag coefficient is defined as $C_D = 8D/\pi$ with $D = \mathbf{e}_x \cdot \int_{\mathcal{S}_b} [-P_0 \mathbf{I} + \frac{1}{Re} (\nabla \mathbf{U}_0 + \nabla \mathbf{U}_0^T)] \cdot \mathbf{n} dS$. Note that in Ref. 27, distances were normalized by the length of the major axis, $2b$, instead of the equivalent diameter, $2(b^2 a)^{1/3}$, so that the corresponding Reynolds number and drag coefficient had to be multiplied by $\chi^{-1/3}$ and $\chi^{2/3}$, respectively, to obtain the values reported in the table.

χ	1			1.75			2.25		
Re	100	400	1000	166	332	830	100	500	1000
Present study	0.374	0.107	0.045	0.518	0.285	0.122	1.097	0.305	0.158
Ref. 27	0.369	0.104	0.045	0.518	0.283	0.121
Ref. 28	0.378	0.107	0.045	0.506	0.280	0.121	1.154	0.306	0.157

B. Perturbations

The governing equations for the $O(\epsilon)$ -perturbations are obtained by linearizing the Navier-Stokes equations around the base state $(\mathbf{U}_0, P_0, \Sigma_0)$ and imposing suitable boundary conditions. The resulting system reads

$$\partial_t \mathbf{u} + \mathbf{u} \cdot \nabla \mathbf{U}_0 + \mathbf{U}_0 \cdot \nabla \mathbf{u} = -\nabla p + Re^{-1} \nabla^2 \mathbf{u}, \quad (3a)$$

$$\nabla \cdot \mathbf{u} = 0, \quad (3b)$$

$$Re^{-1} (\nabla \mathbf{u} + \nabla \mathbf{u}^T) \cdot \mathbf{n} = (\sigma + p) \mathbf{n} \text{ on } \mathcal{S}_b, \quad (3c)$$

$$\mathbf{u} \cdot \mathbf{n} = 0 \text{ on } \mathcal{S}_b, \quad (3d)$$

$$\mathbf{u} = \mathbf{0} \text{ on } \mathcal{S}_{in} \cup \mathcal{S}_h, \quad (3e)$$

$$-p \mathbf{n} + Re^{-1} (\nabla \mathbf{u} + \nabla \mathbf{u}^T) \cdot \mathbf{n} = \mathbf{0} \text{ on } \mathcal{S}_{out}, \quad (3f)$$

where σ denotes the disturbance of the normal stress at the bubble surface. The perturbation is assumed to vanish at the inlet of the domain and on its lateral surface, both being located ‘‘far’’ from the bubble. Given the time and azimuthal invariance of the base flow, the solution of the linearized problem (3) can be sought in the form of normal modes. Defining the state vector $\mathbf{q} = (\mathbf{u}, p, \sigma)$, the normal modes take the form

$$\mathbf{q} = \hat{\mathbf{q}}(r, z) e^{\lambda t + i m \theta} + c.c., \quad (4)$$

where $c.c.$ stands for the complex conjugate, $\lambda = \lambda_r + i \lambda_i$ is the complex growth rate, and m is the azimuthal wavenumber, the unit vector in the azimuthal direction being \mathbf{e}_θ . Symmetry/antisymmetry considerations associated to each value of m directly dictate the suitable boundary condition to be set on the axis \mathcal{S}_a . Defining $\hat{u}_r = \hat{\mathbf{u}} \cdot \mathbf{e}_r$, $\hat{u}_\theta = \hat{\mathbf{u}} \cdot \mathbf{e}_\theta$, $\hat{u}_x = \hat{\mathbf{u}} \cdot \mathbf{e}_x$, one successively finds that the appropriate conditions write $\hat{u}_r = \partial_r \hat{u}_x = \partial_r \hat{p} = 0$ for $m = 0$, $\partial_r \hat{u}_r = \partial_r \hat{u}_\theta = \hat{u}_x = \hat{p} = 0$ for $|m| = 1$ and $\hat{u}_r = \hat{u}_\theta = \hat{u}_x = \hat{p} = 0$ for $|m| \geq 2$.

For each m , the system (3) supplemented with the appropriate boundary conditions on \mathcal{S}_a yields a generalized eigenvalue problem which can be recast in the generic form

$$(\lambda_r + i \lambda_i) \mathcal{B} \hat{\mathbf{q}} + \mathcal{A}_m \hat{\mathbf{q}} = \mathbf{0}. \quad (5)$$

The explicit form of the mass (\mathcal{B}) and stiffness (\mathcal{A}_m) matrices is provided in Eq. (A5) of Appendix A. The generic problem (5) is solved using a shift-invert Arnoldi technique implemented in the SLEPc library.

As usual, the eigenmodes predicted by the LSA are defined up to a multiplicative prefactor and, in order to compare the structure of the various modes, a suitable normalization condition is

required. Following Ref. 29, we normalize each mode in such a way that the lift force it exerts on the bubble is unity.

IV. DISCUSSION OF RESULTS

Since the most amplified disturbance corresponds to the azimuthal wavenumber $m = \pm 1$ we hereinafter focus on this mode. Moreover, the system (3) is invariant through the transformation $(m, \lambda, u_r, u_\theta, u_z, p, \sigma) \rightarrow (-m, \lambda, u_r, -u_\theta, u_z, p, \sigma)$ so that we only discuss the case $m = 1$.

A. Neutral curves

In order to determine the critical values of the control parameters χ and Re at which the base flow loses its stability, we solved the eigenvalue problem (5) for several bubble aspect ratios between 2.1 and 2.55 and various Re . The variations of the growth rate λ_r (and its associated frequency λ_i in the case of unsteady modes) with Re for different values of χ are plotted in Figure 4. For each χ , the curves in this figure evidence a destabilization-restabilization behavior since, increasing Re , the growth rate goes from negative to positive values, reaches a maximum, then decreases and eventually goes back to negative values. This finding confirms that, at variance with rigid bodies, the wake past a fixed-shaped bubble is only unstable within a finite range of Re whose extent increases with the aspect ratio.⁹ These curves also show that the maximum growth rate increases with the aspect ratio, thus defining a critical threshold χ_C for which the maximum growth rate is zero. Hence the wake past bubbles with $\chi < \chi_C$ remains stable whatever Re . Finally, the Strouhal number $St = \lambda_i/(2\pi)$ of the oscillating modes is found to be nearly independent of the Reynolds number.

The neutral curves corresponding to the thresholds of the stationary and oscillating instabilities are plotted in Figure 5 in the form of a (χ, Re) phase diagram. We generally increased the Reynolds number with steps $\Delta Re \simeq 3$, which gives an estimate of the accuracy of these thresholds. The wake becomes globally unstable through a stationary bifurcation for $\chi_{Csta} \simeq 2.21$ at $Re \simeq 400$. However, it starts to oscillate only beyond a second threshold $\chi_{Cosc} \simeq 2.41$ corresponding to the occurrence of a Hopf bifurcation. As shown in the figure, present linear predictions for the threshold of the stationary bifurcation agree well with results from a previous DNS study.⁹ Actually, the agreement is remarkably good in the lower part of the diagram, where the thresholds predicted by the LSA collapse onto those provided by the DNS. We may also point out that the above value of χ_{Csta} is identical to threshold at which path instability was observed to occur in Ref. 7, which suggests a close connection between wake and path instability. Nevertheless, it is still unclear how far this connection extends. Indeed, owing to the additional degrees of freedom and role of body inertia, the path instability problem for a freely moving body generally differs much from the wake

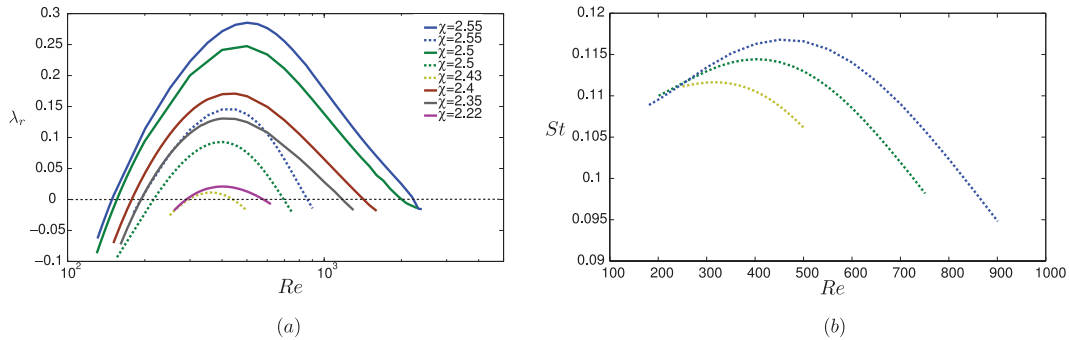


FIG. 4. Variation of (a) the growth rate and (b) the Strouhal number $\lambda_i/(2\pi)$ as a function of the Reynolds number for several bubble aspect ratios. Solid (resp. dashed) lines are associated with stationary (resp. oscillating) modes. In grayscale, the one-to-one correspondence between curves and aspect ratios may be established by noting that the larger the χ , the larger the maximum growth rate and Strouhal number of a given mode.

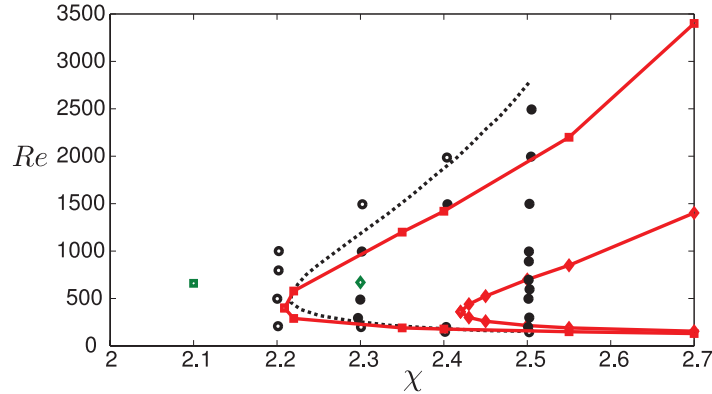


FIG. 5. Phase diagram (χ, Re) showing the neutral curves (in red/solid lines) corresponding to the onset of the stationary (squares) and oscillating (diamonds) modes. Open (resp. closed) circles correspond to DNS results from Ref. 9 in which the wake was observed to be stable (resp. unstable). The dashed line is also from Ref. 9 and was determined by linearly interpolating the growth rates of the neighboring data points. The open square and diamond (green online), respectively, correspond to the threshold of the stationary and oscillating modes determined in Ref. 10 for $Re = 660$.

instability problem for the same body held fixed (see, e.g., Ref. 15 for the case of falling discs). In line with this remark, it is worth pointing out the following. In Refs. 6 and 30, it was observed experimentally that the critical aspect ratio corresponding to the onset of path instability for bubbles having Reynolds numbers of several hundreds is in the range 1.9–2.0, rather than about 2.2 as suggested by Figure 5. However, the reason for this difference is still unclear. It may be merely due to the fact that the fore-aft asymmetry of real bubbles favors path instability, leading to critical aspect ratios smaller than those predicted assuming a perfectly spheroidal shape.³¹ It may also be an effect of intrinsic differences between the path instability and wake instability problems. We have to wait until a LSA of the path instability problem for a freely moving spheroidal bubble will be available (such as that reported in Ref. 14 for two-dimensional plates and rods) to settle the manner definitely.

Returning to Figure 5, significant differences between present predictions and DNS results from Ref. 9 are observed in the upper part of the neutral curve, the return to axisymmetry found in the DNS occurring at values of the Reynolds number noticeably higher than those predicted by the present approach. To explain this discrepancy, we first suspected nonlinear effects; however, using weakly nonlinear analysis in the spirit of Ref. 32, we checked that the bifurcation is supercritical. Given that the two sets of computations have a comparable level of accuracy even at such high Reynolds numbers, the most plausible explanation we see lies in the difference of approach regarding the time evolution of the flow: while the present approach considers the evolution of a perturbation on a strictly stationary base flow governed by (2), both the base flow and the perturbation evolve in time in the DNS. In this range of Re , the time evolution of the base flow, especially that governing the shrinking of the standing eddy, may be very slow, so that the growth or decay of the perturbation observed in the DNS could actually be a transient. We plan to perform new DNS in this range of Re to check this hypothesis.

Finally, a significant difference can be noticed in Figure 5 between the two data points extracted from Ref. 10 (corresponding to $Re = 660$) and present results (which are essentially similar to the DNS results of Ref. 9 in that range of Re). Since the grid and domain sizes as well as the grid resolution in the vicinity of the bubble are similar in Refs. 9 and 10, none of these characteristics can explain the observed differences. It is most likely that the answer lies in an insufficient temporal convergence of the base flow used in Ref. 10. Indeed, Figure 2(b) of that reference indicates that, for all six values of χ under consideration, the viscous component of the drag force is still slowly decreasing at the final time of the computation. This is in line with the values of the drag coefficient reported in Table I of Ref. 10 which are observed to be slightly larger than those found in Refs. 9 and 27.

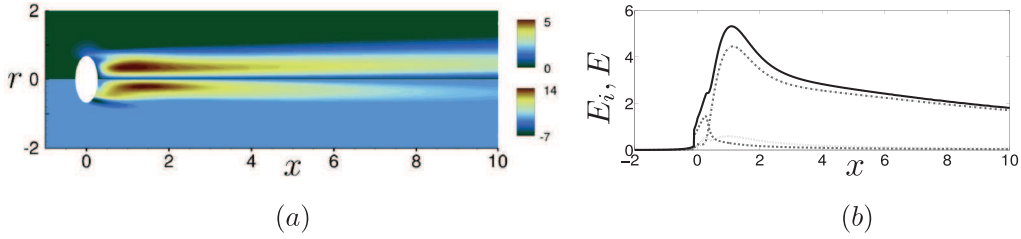


FIG. 6. (a) Axial velocity (upper half) and vorticity (lower half) of the stationary mode $\hat{\mathbf{q}}_{sta-}$ observed at $Re = 155$ for a bubble with $\chi = 2.5$. (b) Energy distribution along the wake: the dotted, dashed, and dashed-dotted lines correspond to the radial, azimuthal, and axial contributions, respectively, while the solid line corresponds to the total energy.

B. Structure of the unstable modes

We now discuss the structure of the unstable global modes. For this purpose, we select the bubble aspect ratio $\chi = 2.5$ for which the stationary and oscillating modes are both unstable within a certain range of Re . Similar mode structures are observed for other aspect ratios. As indicated by Figure 5, the axisymmetric wake first becomes unstable at $Re_{sta-} \simeq 155$ through a stationary bifurcation which breaks the axial symmetry of the base flow. This threshold is in good agreement with the value $Re = 150$ provided by DNS.⁹ Figure 6 shows the structure of this first global mode, hereinafter termed $\hat{\mathbf{q}}_{sta-}$, through isovalues of the axial velocity and vorticity. Owing to the conditions satisfied by the $m = 1$ eigenmodes on the axis \mathcal{S}_a , both quantities are antisymmetrical with respect to this axis. The structure of this mode is thus characterized by two counter-rotating streamwise vortices, as already observed with other axisymmetric bodies, i.e., rigid disks and spheres^{21,33,34} as well as bubbles.^{9,10} The energy of each component of the velocity, $E_i(x) = \int_0^h |\hat{\mathbf{u}}_i(r, x)|^2 r dr$, where the suffix i stands for (r, θ, z) , and the total energy, $E(x) = E_r(x) + E_\theta(x) + E_x(x)$, are displayed in Figure 6(b). The contribution of the streamwise component, which reaches a maximum in the standing eddy and then decreases slowly downstream, is clearly dominant.

A secondary bifurcation of Hopf type is found to take place at $Re_{osc-} \simeq 215$. It corresponds to the growth of an oscillating mode, hereinafter termed $\hat{\mathbf{q}}_{osc-}$. This mode preserves the planar symmetry of the wake and exhibits an alternation of positive and negative streamwise vorticity on both sides of the symmetry plane. The corresponding frequency, $St \sim 0.110$, is in good agreement with the DNS prediction⁹ ($St \sim 0.116$). However, the value of Re_{osc-} is significantly larger than the DNS prediction $Re = 195$. This is very likely due to the fact that the prediction provided by the LSA is obtained by considering an axisymmetric base flow, while the actual base flow is not axisymmetric any more. Similar differences between LSA³³ and DNS²⁹ predictions have been observed with spheres and disks, the threshold predicted in the latter being always lower than that predicted by the linear approach.

Figure 7 shows that positive and negative values alternate periodically in the spatial structure of the real part of $\hat{\mathbf{q}}_{osc-}$. The corresponding energy distribution differs from that of the previous mode, though the streamwise component is still dominant. Here, energy increases monotonically in the

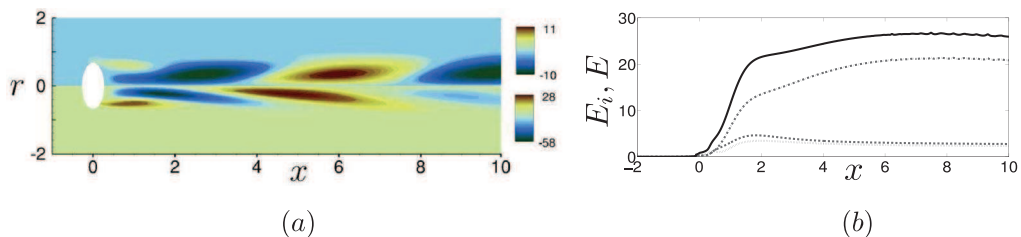


FIG. 7. (a) Axial velocity (upper half) and vorticity (lower half) of the oscillating mode $\hat{\mathbf{q}}_{osc-}$ observed at $Re = 215$ for a bubble with $\chi = 2.5$. (b) Energy distribution along the wake (same convention as in Figure 6).

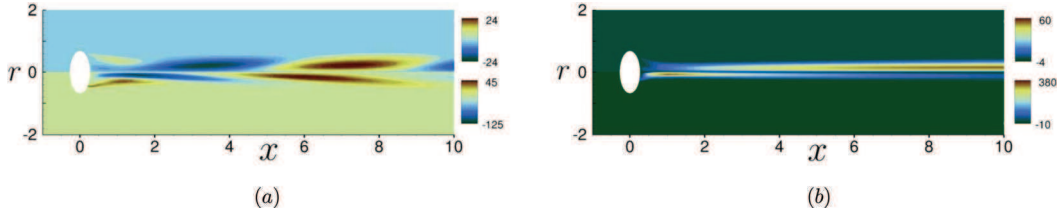


FIG. 8. Axial velocity (upper half) and vorticity (lower half) in the wake of a bubble with $\chi = 2.5$. (a) $\hat{\mathbf{q}}_{osc^+}$ mode at $Re = 700$; (b) $\hat{\mathbf{q}}_{sta^+}$ mode at $Re = 2000$. The high values reached by the velocity and vorticity of these modes indicate that the lift force acting on the bubble (used to define their normalization) is quite small in this high- Re regime.

downstream direction, although the slope is much weaker downstream of the standing eddy. This behavior is reminiscent from that observed in the wake of a rigid sphere.²¹

It is of interest to examine the structure of the modes predicted by the LSA in the range of Re corresponding to the restabilization of the wake, i.e., to the upper part of the neutral curves in Figure 5, keeping in mind that there may be some differences between the actual base flow and the axisymmetric steady flow used in the LSA near the upper threshold Re_{osc^+} of the oscillating mode. For a bubble with $\chi = 2.5$, stationarity is recovered at $Re_{osc^+} \approx 700$. The corresponding mode, $\hat{\mathbf{q}}_{osc^+}$, is displayed in Figure 8(a). It exhibits elongated vortical patches which tend to align with the symmetry axis of the base flow; the corresponding Strouhal number is about 0.102. Still increasing Re , axisymmetry is recovered for $Re_{sta^+} \approx 2000$. The corresponding stationary mode, $\hat{\mathbf{q}}_{sta^+}$, has a very flattened structure and the streamwise vortices are almost “glued” to the symmetry axis.

Although the restabilization process takes place at Reynolds numbers much larger than the threshold of the first instability, Re_{sta^-} , it is no surprise that the LSA predicts its occurrence and the range of Re where the flow returns to axisymmetry. The reason is that the restabilization mechanism is entirely governed by a key property of the base flow resulting from the shear-free condition (2c). Indeed, as shown in Ref. 9, this condition implies that the vorticity flux entering the flow scales as $Re^{-1/2}$ for $Re \rightarrow \infty$, instead of remaining of $O(1)$ at a no-slip surface. Hence, when Re is large enough, the base flow past the bubble becomes closer and closer to a potential flow as Re goes on increasing, and recovers its stability irrespective of any nonlinear mechanism.

V. RECEPTIVITY AND SENSITIVITY TO EXTERNAL DISTURBANCES

A. Adjoint modes

In order to locate precisely the core of the first instability and to identify the specificities of bubble wake instability compared to that of a rigid body, we rely on the concept of “wavemaker” widely used in open flows³⁵ and more recently applied to afterbody wakes.^{17,19,21} The so-called wavemaker is the region of the flow which is most sensitive to small modifications of the linear operator \mathcal{A}_m in Eq. (5). A small perturbation of \mathcal{A}_m inducing a change in the spectrum of the operator, the wavemaker zone can also be identified as the locus of the points where the amplification of the most unstable mode is maximum. Following recent work on afterbody wakes,^{17,19–22} we use a linear adjoint-based approach to determine this region. This approach is now quite standard and only the main steps required by the derivation are given here. More detail can be found in the aforementioned papers and in other references by the same groups.

We first classically define the inner product between two vector fields \mathbf{a} and \mathbf{b} as

$$\langle \mathbf{a}, \mathbf{b} \rangle = \int_{\mathcal{D}} \mathbf{a}^* \cdot \mathbf{b} r dr dz, \quad (6)$$

where $*$ and (\cdot) denote to the complex conjugate and the standard Hermitian product, respectively. Then, the adjoint mode $\hat{\mathbf{q}}^\dagger$ is the solution of the adjoint eigenvalue problem:

$$(\lambda_r - i\lambda_i)\mathcal{B}\hat{\mathbf{q}}^\dagger + \mathcal{A}_m^\dagger\hat{\mathbf{q}}^\dagger = \mathbf{0}, \quad (7)$$

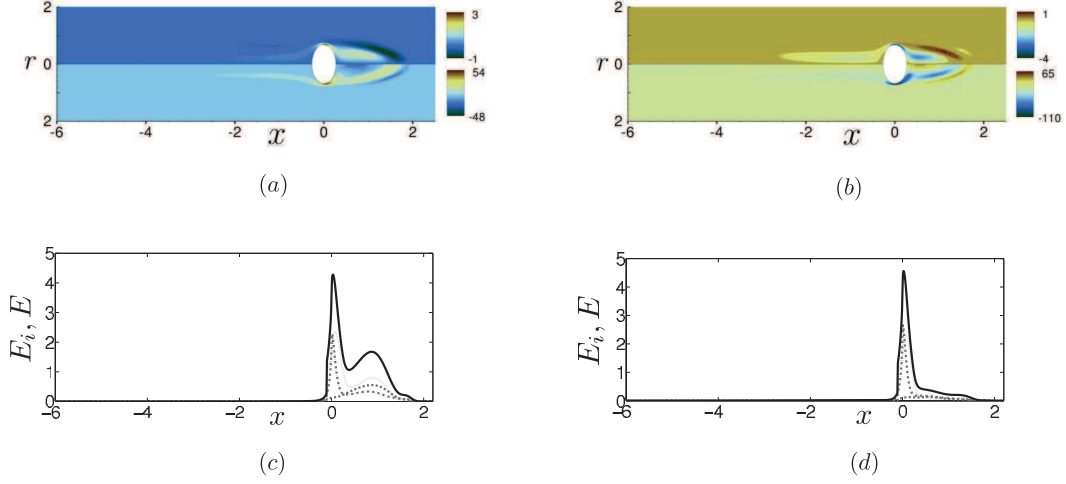


FIG. 9. (Top) Axial velocity (upper half) and vorticity (lower half) of the adjoint modes: (a) stationary mode computed at $Re = Re_{Csta-} = 155$ and (b) oscillating mode computed at $Re = Re_{Cosc-} = 215$. (Bottom) Energy distribution of the adjoint modes along the wake: (c) stationary mode and (d) oscillating mode (see Figure 6 for caption).

where \mathcal{A}_m^\dagger satisfies $\langle \hat{\mathbf{q}}^\dagger, \mathcal{A}_m \hat{\mathbf{q}} \rangle = \langle \mathcal{A}_m^\dagger \hat{\mathbf{q}}^\dagger, \hat{\mathbf{q}} \rangle$. The adjoint operator \mathcal{A}_m^\dagger is found by integrating the left-hand-side of Eq. (5) by parts, with the resulting boundary terms required to vanish.³⁶ In detailed form, the adjoint mode is the solution of the set of equations:

$$\partial_r \mathbf{u}^\dagger + \mathbf{u}^\dagger \cdot \nabla \mathbf{U}_0^T - \mathbf{U}_0 \cdot \nabla \mathbf{u}^\dagger = \nabla p^\dagger + Re^{-1} \nabla^2 \mathbf{u}^\dagger, \quad (8a)$$

$$\nabla \cdot \mathbf{u}^\dagger = 0, \quad (8b)$$

$$Re^{-1} (\nabla \mathbf{u}^\dagger + \nabla \mathbf{u}^{\dagger T}) \cdot \mathbf{n} = -(\sigma^\dagger + p^\dagger) \mathbf{n} \text{ on } \mathcal{S}_b, \quad (8c)$$

$$\mathbf{u}^\dagger \cdot \mathbf{n} = 0 \text{ on } \mathcal{S}_b, \quad (8d)$$

$$\mathbf{u}^\dagger = \mathbf{0} \text{ on } \mathcal{S}_{in}, \quad (8e)$$

$$u_r^\dagger = \partial_r u_\theta^\dagger = \partial_r u_x^\dagger = 0 \text{ on } \mathcal{S}_h, \quad (8f)$$

$$p^\dagger \mathbf{n} + Re^{-1} (\nabla \mathbf{u}^\dagger + \nabla \mathbf{u}^{\dagger T}) \cdot \mathbf{n} + (\mathbf{U}_0 \cdot \mathbf{n}) \mathbf{u}^\dagger = \mathbf{0} \text{ on } \mathcal{S}_{out}. \quad (8g)$$

The boundary conditions on the axis \mathcal{S}_a are similar to those imposed to the direct mode corresponding to $m = 1$.

Figure 9 shows the structure of the adjoint global modes, each computed at the threshold of the corresponding instability (both modes are normalized in such a way that $\langle \hat{\mathbf{q}}^\dagger, \mathcal{B} \hat{\mathbf{q}} \rangle = 1$). These modes are clearly intense essentially within the standing eddy and keep a significant magnitude over some distance upstream of the bubble. The latter trend is typical of open flows and wakes; it is known to be due to the convective non-normality of the linearized Navier-Stokes operator.³⁵ The energy distribution of $\hat{\mathbf{q}}_{sta-}^\dagger$ reaches a maximum in the core of the recirculation zone while that of $\hat{\mathbf{q}}_{osc-}^\dagger$ exhibits a clear maximum near the separation line. These distributions also reveal that the streamwise component is no longer the dominant contribution in the total energy. Instead, the cross-stream components dominate, especially in the stationary mode. This feature, known as lift-up non-normality,³⁵ is also generic of open flows.

The adjoint mode represents the most dangerous initial disturbance of unit norm,^{35,36} i.e., the one maximizing the flow kinetic energy at large time if the flow is unstable. In order to gain more

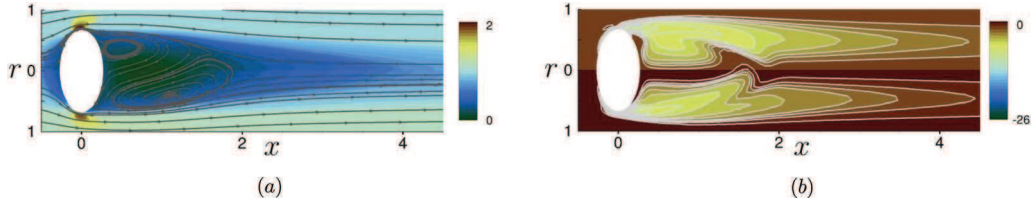


FIG. 10. The total flow around a bubble with $\chi = 2.5$ at $Re = 155$: (a) iso-contours of the axial velocity and streamlines; (b) iso-contours of the azimuthal vorticity.

insight into the nature of this initial disturbance, we computed the total flow $\hat{\mathcal{Q}} = \hat{\mathcal{Q}}_0 + \epsilon \hat{\mathbf{q}}_{sta-}^\dagger$, where $\hat{\mathcal{Q}}_0$ represents the mode associated with the base flow. For this purpose ϵ was set to $\simeq 0.08$, so that the adjoint mode represents 1% of the energy of the base flow. Figure 10(a) shows that the optimal disturbance for the primary instability to set in consists of a steady displacement of the separation line, similar to what has been observed for the flow past a rigid sphere.²¹ The top and bottom points of the separation line move to $(x = 0.19, r = 0.49)$ and $(x = 0.14, r = 0.59)$, respectively, resulting in an inclination of the standing eddy. Furthermore, Figure 10(b) shows how the optimal disturbance deforms the vorticity isolines in the flow. Of particular interest is the shape of these isocontours in the upper part of the figure, just at the back of the bubble. In this subregion it may be seen that the angle θ_ω between the isocontours and the symmetry axis of the base flow is just below 90° . In Ref. 9 it was argued that, for large enough Re and whatever the boundary condition (i.e., no-slip or shear-free) at the body surface, the flow in the recirculating region past an axisymmetric body becomes unstable when $\theta_\omega < 90^\circ$ because vorticity transport by the base flow can then only be balanced by streamwise viscous diffusion, leading to stronger and stronger streamwise vorticity gradients as Re increases (no recirculating region past a shear-free bubble exists when $Re \rightarrow \infty$, so that in this case the above scenario applies to the interval of intermediate values of Re within which this region has a finite extent; in other terms, when Re is said to be “large” or to “increase” in the above argument, it must be kept in mind that this Re is still smaller than the critical Reynolds number beyond which no recirculating region exists). Although the amplitude of the disturbance in Figure 10(b) is arbitrary, the tendency for $\hat{\mathbf{q}}_{sta-}^\dagger$ to make the angle θ_ω become acute is clear and fully supports this scenario.

B. Receptivity to a localized feedback

The adjoint mode is particularly helpful in determining the so-called flow receptivity. Following Ref. 17, we first define the “wavemaker” as the region most sensitive to a local force-velocity coupling of the form

$$\hat{\mathbf{f}} = \mathbf{C} \cdot \hat{\mathbf{u}} \delta(x - x_0, r - r_0), \quad (9)$$

where \mathbf{C} is the 3×3 matrix expressing the coupling. Since it may be shown¹⁷ that the eigenvalue drift $\delta\lambda$ obeys the inequality $|\delta\lambda| \leq \|\mathbf{C}\| \|\hat{\mathbf{u}}\| \|\hat{\mathbf{u}}^\dagger\| \langle \hat{\mathbf{u}}^\dagger, \hat{\mathbf{u}} \rangle^{-1}$, we take advantage of the normalization condition defined above and determine the region where the magnitude of $\delta\lambda$ is maximum by simply computing the quantity $\beta = \|\hat{\mathbf{u}}\| \|\hat{\mathbf{u}}^\dagger\|$ at every point of the flow field.

Figure 11 displays $\beta(r, x)$ in the vicinity of the bubble. It reveals that the wavemaker is located in a region whose extension is close to that of the standing eddy in the corresponding base flow, a property resulting from the spatial separation of the direct and adjoint modes. The wavemaker associated with the first global mode (Figure 11(a)) is the most intense and reaches its highest values near the center of the standing eddy. Moreover, the comparison with Figure 11(b) indicates that its structure is very similar to that of the wavemaker in the wake of a rigid sphere at the corresponding threshold. This similarity reinforces the view expressed in Ref. 9 that the mechanism driving the first instability of axisymmetric wakes is *qualitatively* independent of the boundary condition at the body surface (i.e., no-slip vs. shear-free), *quantitative* differences in the thresholds being just a consequence of the different amounts of vorticity produced at the body surface for a given Re . However, a closer look at the two figures reveals a subtle difference between the two types of bodies.

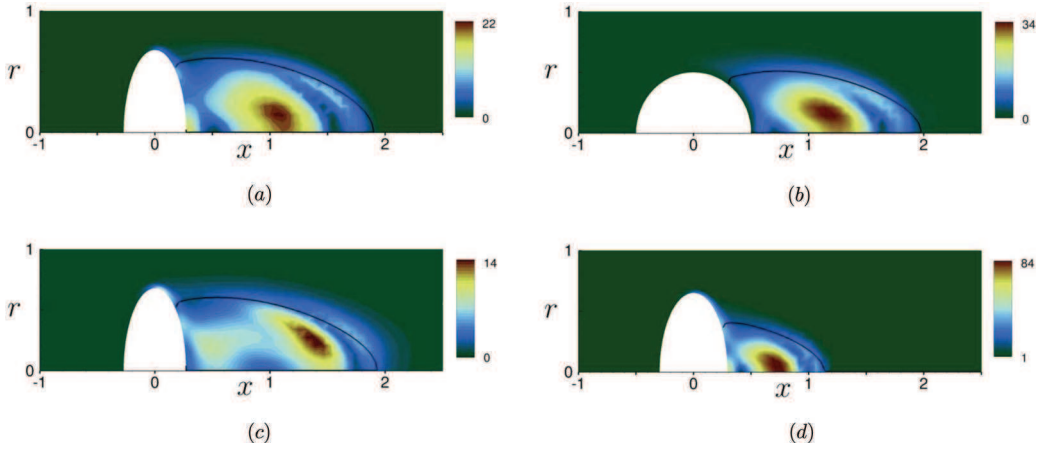


FIG. 11. Sensitivity to a localized feedback expressed through the quantity $\beta(r, x)$. (a) (resp. (c)) stationary (resp. oscillating) mode for a bubble with $\chi = 2.5$ and $Re = 155$ (resp. $Re = 215$); (b) stationary mode for a solid sphere at $Re = 212.9$; (d) stationary mode for a bubble with the critical aspect ratio $\chi = \chi_{Csta} = 2.21$ at $Re = 400$. The solid line marks the separation line.

Indeed, $\beta(r, x)$ keeps significant values all along the rear half of the bubble surface and its distribution exhibits a secondary maximum right at the rear of the bubble near the symmetry axis. These features suggest that a disturbance applied on the rear part of the bubble surface, especially close to its symmetry axis, should significantly modify the stability of the wake. It may also be related to the well-known sensitivity of bubble paths to the presence of minute amounts of surfactants which are swept to the rear of the bubble by the base flow and modify the boundary condition, from shear-free to no-slip, in that region.^{12,30}

There is a striking difference between the spatial structures of the wavemaker intensity in Figures 11(a) and 11(c): in contrast with previous observations for the stationary mode, the latter reveals that the sensitivity to local feedback of the oscillating mode is maximum near the separation line. A similar feature has been noticed in sensitivity analyses of the flow past a two-dimensional cylinder,^{17,19} as well as for axisymmetric bodies such as a sphere and a disk.²¹ Therefore, it appears to be a generic characteristic of shear layer instabilities associated with a Hopf bifurcation. Again, the nature of the body surface does not change qualitatively the overall picture.

Figure 11(d) shows the distribution of $\beta(r, x)$ for a bubble corresponding to the vertex of the neutral curve in Figure 5, i.e., $\chi = 2.2$ and $Re = 395$. The maximum of β is found to be much larger than that in Figure 11(a), indicating that the sensitivity of the stationary mode to a localized feedback increases as χ decreases.

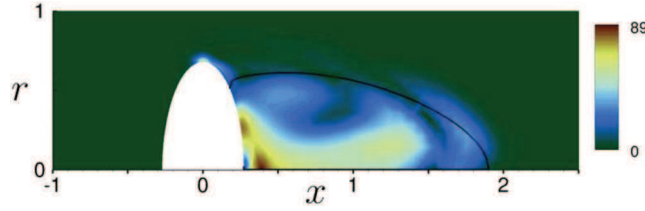
C. Sensitivity to base flow modifications

The above definition of the “wavemaker” leaves aside the role of the base flow in the determination of the most sensitive regions. To reveal this role, we now consider a more elaborate approach in which the “wavemaker” is defined as the zone where the modification of the base flow produces the largest eigenvalue drift.^{19,20,24}

The drift $\delta\lambda$ of an eigenvalue caused by a modification δQ_0 in the base flow is defined as

$$\delta\lambda = \langle \nabla_{Q_0} \lambda, \delta Q_0 \rangle, \quad (10)$$

where the components of the gradient vector $\nabla_{Q_0} \lambda = (\nabla_{u_0} \lambda, \nabla_{p_0} \lambda, \nabla_{\Sigma_0} \lambda)^T$ express the sensitivity of the eigenvalue λ to modifications of the base velocity, pressure, and surface normal stress fields, respectively. These components can be explicitly evaluated using Lagrangian functional

FIG. 12. Spatial distribution of the magnitude of the sensitivity function $\nabla_{Q_0} \lambda_r$.

analysis.^{19,24,37} This approach is detailed in Appendix C where Eq. (C5) provides

$$\nabla_{Q_0} \lambda = -\partial_{Q_0}(\mathcal{A}_1 \hat{\mathbf{q}})^\dagger \cdot \hat{\mathbf{q}}^\dagger \quad (11a)$$

$$= (\hat{\mathbf{u}}^* \cdot \nabla \hat{\mathbf{u}}^\dagger - \hat{\mathbf{u}}^\dagger \cdot \nabla \hat{\mathbf{u}}^*, 0, 0)^T. \quad (11b)$$

Equation (11b) shows that the sensitivities to the pressure and normal stress of the base flow are nil and hence do not contribute to the linear problem (3). It also indicates that the sensitivity to changes in the base velocity field involves two contributions frequently referred to as sensitivity to changes in the production and advection, respectively, since the former (resp. latter) originates from the term $\hat{\mathbf{u}} \cdot \nabla \mathbf{U}_0$ (resp. $\mathbf{U}_0 \cdot \nabla \hat{\mathbf{u}}$) in Eq. (3a). Instability is locally convective in regions where the latter dominates over the former and absolute in the opposite case.³⁸

Figure 12 shows the sensitivity of the growth rate $\nabla_{Q_0} \lambda_r = \mathcal{R}e(\nabla_{Q_0} \lambda)$ to a base flow modification. It turns out that this quantity is maximum when a modification of the base flow is applied in one of three small regions at the rear of the bubble. The first two of these are located right at the bubble surface, one at its top (i.e., on the equatorial plane), the other near the middle of its rear half. The last one, which is also the most intense, lies barely downstream, along the symmetry axis of the base flow.

So far we did not specify the imposed external forcing but rather considered an arbitrary change in the base flow. If the form of the forcing $\delta \mathcal{G}$ is specified, one can directly write $\delta \lambda = \langle \nabla_{\mathcal{G}} \lambda, \delta \mathcal{G} \rangle$ where $\nabla_{\mathcal{G}} \lambda$ defines the sensitivity of the flow to the external forcing. As long as this forcing acts directly on the variables $(\mathbf{U}_0, P_0, \Sigma_0)$ defining Q_0 , it is a simple matter to show^{19,24} (see also Eq. (C12) in Appendix C) that this newly defined sensitivity and the above sensitivity to base flow modifications are directly related through

$$\mathcal{A}_0 \delta Q_0 = \delta \mathcal{G} \quad \text{so that} \quad \mathcal{A}_0^\dagger \nabla_{\mathcal{G}} \lambda = \nabla_{Q_0} \lambda, \quad (12)$$

where \mathcal{A}_0 refers to the linear axisymmetric operator of Eq. (5) corresponding to $m = 0$. In what follows we consider a slightly different form of the forcing involving components acting within the bulk of the base flow and surface components acting directly on the boundary conditions at the bubble surface. More precisely, we set $\mathcal{G} = (\mathcal{F}_0, 0, 0, W_0, \tau_0)^T$ which corresponds to a forcing induced by a momentum variation ($\delta \mathcal{F}_0$) in the bulk, or by variations in the normal velocity (δW_0) or in the shear stress ($\delta \tau_0$) at the bubble surface. Owing to incompressibility, we do not consider a possible source of volume, nor do we apply a forcing directly through the normal stress Σ_0 at the bubble surface, although Σ_0 and W_0 are closely related as shown by the second of Eqs. (14) below. Note that in previous studies,^{16,17,24} the surface (or “wall”) forcing was obtained only through a disturbance applied to the normal velocity (resulting in blowing or suction), whereas the present formulation allows us to study also the effect of a disturbance in the surface shear stress. Here, blowing or suction is of course irrelevant since we are dealing with a bubble and not with a rigid body. However, considering a forcing via the normal velocity at the bubble surface is physically meaningful, since it provides insight into the consequences of a small quasi-steady local deformation of the bubble, corresponding to an increase ($W_0 > 0$) or decrease ($W_0 < 0$) of its local radius (obviously this forcing must be designed in such a way that the volume of the bubble is conserved, so that incompressibility is still satisfied in the surrounding fluid).

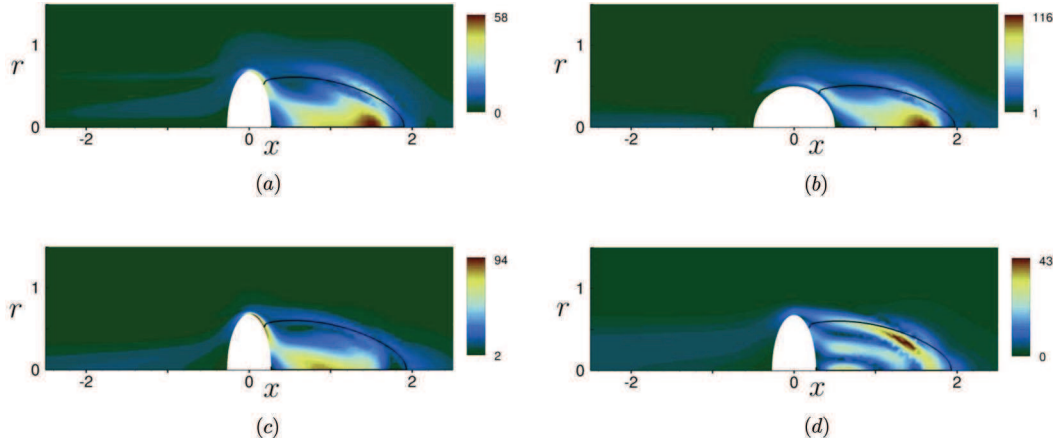


FIG. 13. Distribution of the magnitude of the sensitivity function $\nabla_{\mathcal{F}_0} \lambda$: (a) sensitivity of λ_{sta-} for a bubble with $\chi = 2.5$ at $Re = 155$; (b) same for a rigid sphere at $Re = 212.9$; (c) sensitivity of $\mathcal{Re}(\lambda_{osc-})$ for a bubble with $\chi = 2.5$ at $Re = 215$; (d) same for $\mathcal{Im}(\lambda_{osc-})$.

Introducing the “surface” inner product $\langle \mathbf{a}, \mathbf{b} \rangle_{\mathcal{S}} = \int_{\mathcal{S}_b} \mathbf{a}^* \cdot \mathbf{b} r dl$, where $dl = (dx^2 + dr^2)^{1/2}$, the eigenvalue drift due to the external forcing may be written in the form

$$\delta \lambda = \langle \nabla_{\mathcal{F}_0} \lambda, \delta \mathcal{F}_0 \rangle + \langle \nabla_{W_0} \lambda, \delta W_0 \rangle_{\mathcal{S}} + \langle \nabla_{\tau_0} \lambda, \delta \tau_0 \rangle_{\mathcal{S}}. \quad (13)$$

Again, Lagrangian functional analysis may be used to obtain explicit expressions for the sensitivities to an external forcing. Details of the calculation are provided in Appendix C and the final result (Eq. (C10)) reads

$$\nabla_{\mathcal{F}_0} \lambda = \mathbf{U}_0^\dagger, \quad \nabla_{W_0} \lambda = -\Sigma_0^\dagger, \quad \nabla_{\tau_0} \lambda = \mathbf{U}_0^\dagger \cdot \mathbf{t}, \quad (14)$$

where $\mathbf{t} = \mathbf{n} \times \mathbf{e}_\theta$ is the unit vector locally tangent to the bubble surface and \mathbf{U}_0^\dagger (resp. Σ_0^\dagger) denotes the adjoint of the base velocity field (resp. surface normal stress); the definition of the adjoint base flow is detailed in Appendix C.

The magnitude of the sensitivity function $\nabla_{\mathcal{F}_0} \lambda$ is plotted in Figure 13. Again this figure shows that the standing eddy (especially the subregion located along the symmetry axis) is the most receptive region of the flow. A close examination at Figures 13(a), 13(c), and 13(d) reveals that the upstream part of the flow keeps a non-zero, albeit small, sensitivity. However, the main information conveyed by this figure is obtained by comparing plots (a) and (c) with plot (b): in contrast with the surface of the rigid sphere, the bubble surface, especially the region just at the back of the equator, is observed to exhibit a significant sensitivity (actually the sensitivity even reaches its maximum in that region for the oscillating mode). Therefore, a base flow disturbance applied right on this part of the surface is expected to modify significantly the growth rate of both modes.

Variations of the two surface components of the sensitivity, $\nabla_{W_0} \lambda$ and $\nabla_{\tau_0} \lambda$, are plotted as a function of the polar angle α in Figure 14. The real part of the sensitivity to the tangential stress, $\mathcal{Re}(\nabla_{\tau_0} \lambda)$, exhibits a quite similar shape for both modes but the maximum sensitivity is about twice as large for the oscillating mode. It is positive throughout the bubble surface, indicating that a positive $\delta \tau_0$ (corresponding to a shear acting in the downstream direction, from $\alpha = 180^\circ$ to $\alpha = 0^\circ$) is always destabilizing. This sensitivity increases regularly from the rear stagnation point to its maximum, reached for $\alpha \approx 75^\circ$ for both modes, a location which almost coincides with the position of the separation line. Then $\mathcal{Re}(\nabla_{\tau_0} \lambda)$ progressively returns to zero on the front part of the surface. Hence, in case $\delta \tau_0$ would result from the presence of an insoluble surfactant at the bubble surface, the contaminated region that would contribute most to the destabilization of the flow would be that corresponding to the broad maximum of $\mathcal{Re}(\nabla_{\tau_0} \lambda)$, say $35^\circ \leq \alpha \leq 90^\circ$. As shown by Figure 14(c), the imaginary part corresponding to the oscillating mode is negative in the range $15^\circ \leq \alpha \leq 70^\circ$ approximately, so that a positive $\delta \tau_0$ applied in this region would lower the frequency of this mode, especially if the forcing were applied around $\alpha = 40^\circ$. In contrast it would increase

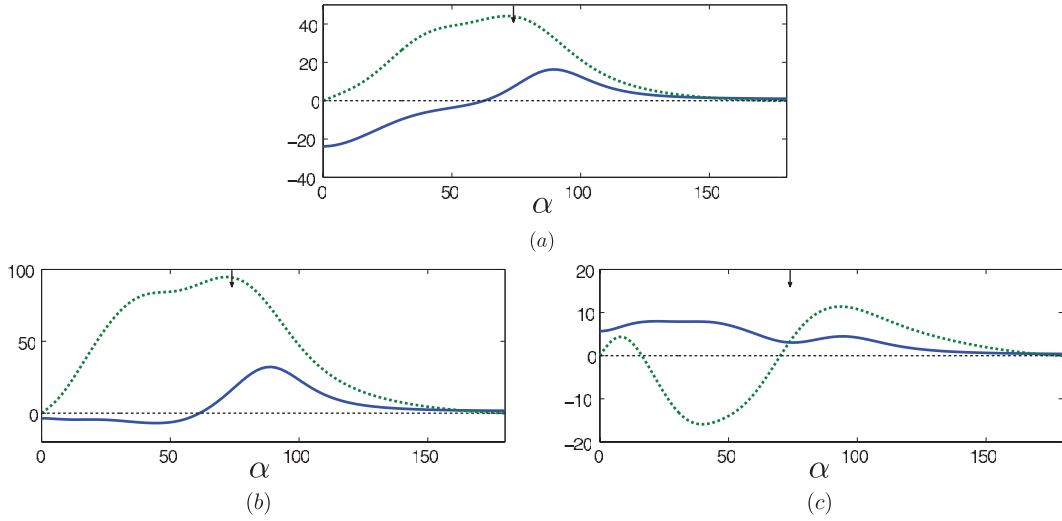


FIG. 14. Profiles of the sensitivity functions $\nabla_{W_0}\lambda$ (blue/solid line) and $\nabla_{\tau_0}\lambda$ (green/dashed line) along the surface for a bubble with $\chi = 2.5$: (a) λ_{sta-} at $Re = 155$; (b) (resp. (c)) real (resp. imaginary) part for λ_{osc-} at $Re = 215$. The polar angle α goes from 0° at the rear of the bubble to 180° at its front; the arrow indicates the position of the separation angle.

the frequency if standing somewhere else on the surface, especially near the equator of the bubble where $\mathcal{I}m(\nabla_{\tau_0}\lambda)$ reaches its maximum.

The real part of the sensitivity to the normal velocity, $\mathcal{R}e(\nabla_{W_0}\lambda)$, changes sign at $\alpha \approx 60^\circ$ for both modes. It is negative over most of the surface area on which the flow recirculates, indicating that a local expansion of the bubble in that region would be stabilizing, especially in the vicinity of the first threshold (Figure 14(a)) for which the sensitivity is found to take large negative values close to the rear stagnation point ($\alpha = 0^\circ$). Obviously the corresponding mechanism is similar to the well-known stabilizing effect of blowing (the so-called “base bleed”) on blunt trailing edges.^{23,24,39} For positions such that $\alpha > 60^\circ$, $\mathcal{R}e(\nabla_{W_0}\lambda)$ is positive and reaches its maximum on the equator of the bubble for both modes, until gently decreasing to zero on the front half of the surface. Again, the maximum sensitivity of the oscillating mode is nearly twice as large as that of the stationary mode. It must be kept in mind that, although Figure 14(a) may give the impression that applying a uniform $W_0 > 0$ throughout the bubble surface would result in a negative average value of $\mathcal{R}e(\nabla_{W_0}\lambda)$, this surface-averaged sensitivity would actually be positive, i.e., this uniform growth of the bubble would be destabilizing, owing to the axisymmetric geometry which makes the contribution of regions close to the equator dominant. This is in line with the fact that uniform blowing lowers the thresholds of the first two transitions of the flow past a sphere.⁴⁰ Last, Figure 14(c) reveals that a positive W_0 increases the frequency of the oscillating mode whatever the position of the forcing, the effect being maximum when the forcing stands in the central part of the recirculating region, in the range $20^\circ \leq \alpha \leq 50^\circ$. As a final remark, it is probably interesting to notice the following. Considering an initially spheroidal bubble with a given equatorial diameter (i.e., $W_0 = 0$ for $\alpha = 90^\circ$), Figures 14(a) and 14(b) indicate that the stability of the flow about it would be improved by applying a negative (resp. positive) normal velocity on its front (resp. rear) part, leading gradually to a bubble with a flatter front and a more rounded rear (but with the same volume as the initial spheroidal bubble). This slightly deformed shape coincides qualitatively with that of actual millimeter-size bubbles whose fore-aft asymmetry resulting from small viscous effects is well known.⁶ Hence, other things being equal, the axisymmetric flow past a rising bubble with a slowly growing fore-aft asymmetry is expected to be slightly more stable than that past the oblate spheroidal model considered here. Note that this situation involving a slowly *time-evolving* bubble shape differs from the one recently considered in Ref. 31 where the stability properties of the flow past two bubbles having the same volume and two different *frozen* shapes, one being perfectly spheroidal, the other exhibiting a realistic fore-aft asymmetry, were compared.

D. Effects of a localized quadratic forcing

Previous results provide interesting information regarding the sensitivity of the first two eigenpairs taken at their respective threshold. Nevertheless they do not allow us to determine how these variations affect the growth rate and frequency of the corresponding modes. To make some progress on this question, we finally follow recent attempts devoted to passive control by small devices^{24,43} and consider that the *total* flow $\mathbf{U} = \mathbf{U}_0 + \epsilon \mathbf{u}$ is disturbed by a localized quadratic force placed on the axis of the base flow, namely,

$$\delta \mathcal{F} = -\frac{\pi}{8} C_x \frac{l^2}{d^2} \|\mathbf{U}\| \mathbf{U} \delta(r, x - x_0). \quad (15)$$

This force can be seen as the reaction exerted on the flow by a small axisymmetric body of dimensional cross section $\pi l^2/4$ and drag coefficient C_x located at $r = 0, x = x_0$. This body can be thought of as a second bubble or a rigid particle standing near the test bubble in an in-line configuration. The following analysis assumes implicitly that $ld \ll 1$ (so that there is no deviation of the base flow by the added body) and that the Reynolds number $Re_l = \|\mathbf{U}\|l/\nu$ is sufficiently small for the wake past the added body to be intrinsically stable. Assuming that C_x does not vary significantly with Re_l when $Re_l \approx Re_l^0 = \|\mathbf{U}_0\|l/\nu$, one has

$$\delta \mathcal{F} = -C \|\mathbf{U}\| \mathbf{U} \delta(r, x - x_0) \simeq -C \left\{ \underbrace{\|\mathbf{U}_0\| \mathbf{U}_0}_{\delta \mathcal{F}_0} + \epsilon \underbrace{\left(\|\mathbf{U}_0\| \hat{\mathbf{u}} + \frac{\mathbf{U}_0 \cdot \hat{\mathbf{u}}}{\|\mathbf{U}_0\|} \mathbf{U}_0 \right)}_{\delta \hat{\mathbf{f}}} e^{\lambda t} \right\} \delta(r, x - x_0), \quad (16)$$

where $C = (\pi/8)(l/d)^2 C_x (Re_l^0)$. In Eq. (16) $\delta \mathcal{F}_0$ and $\delta \hat{\mathbf{f}}$ represent the action of the force through the base flow and the global mode, respectively. Note that the latter involves two contributions, one related to the change of magnitude of \mathbf{U} , the other to its change of direction. While $\delta \mathcal{F}_0$ is always steady, $\delta \hat{\mathbf{f}}$ can either be steady or oscillating at the frequency of the global mode, depending on the nature of the mode under consideration. Splitting the eigenvalue drift in the form $\delta \lambda = \delta_{\mathcal{F}_0} \lambda + \delta_{\hat{\mathbf{f}}} \lambda$, relying on Eq. (14) and on its counterpart for the global mode,²⁴ namely, $\nabla_{\hat{\mathbf{f}}} \lambda = \hat{\mathbf{u}}^\dagger$, yields

$$\delta_{\mathcal{F}_0} \lambda = -C \|\mathbf{U}_0\| \mathbf{U}_0^\dagger \cdot \mathbf{U}_0, \quad (17a)$$

$$\delta_{\hat{\mathbf{f}}} \lambda = -C \|\mathbf{U}_0\| \left(\hat{\mathbf{u}}^\dagger \cdot \hat{\mathbf{u}} + \frac{\mathbf{U}_0 \cdot \hat{\mathbf{u}}}{\|\mathbf{U}_0\|^2} \hat{\mathbf{u}}^\dagger \cdot \mathbf{U}_0 \right). \quad (17b)$$

Varying the position x_0 then allows us to obtain the variations of the growth rate and (possibly) those of the frequency of a given eigenmode at the corresponding threshold by extracting the real and imaginary parts of Eqs. (17), respectively. Predictions could also be obtained further away from the threshold by properly varying C so as to take variations of C_x with Re_l into account.

Figure 15 shows how the forcing affects the eigenvalues close to the first two bifurcation thresholds. Note that no value has been assigned to C , so that the magnitudes displayed in the various subfigures are actually normalized by C . A small spherical bubble (resp. rigid sphere) with $ld = 1/10$ would have a Reynolds number close to 15 for $Re \approx Re_{sta^-}$, thus a drag coefficient about 1.75 (resp. 3.5),⁴⁴ leading to $C \approx 7 \times 10^{-3}$ (resp. 1.4×10^{-2}). Hence the actual variations of the eigenvalues are typically two orders of magnitude smaller than the normalized variations displayed in Figure 15.

Comparison of Figures 15(a) and 15(b) regarding the stationary mode reveals that effects of the forcing are qualitatively similar for a bubble and a rigid sphere as long as this forcing is located within the standing eddy. More precisely, the disturbance is destabilizing, both through the base flow and the global mode, when the forcing is applied either very close to the back of the body (as we already observed in Figure 12) or close to the separation line, the destabilizing effect being smaller in the latter case. In contrast, the forcing is strongly stabilizing when applied in the core of the standing eddy. A surprising feature occurs when the forcing is applied at some distance upstream of the body: while this situation is found to stabilize the flow past the rigid sphere, it is observed

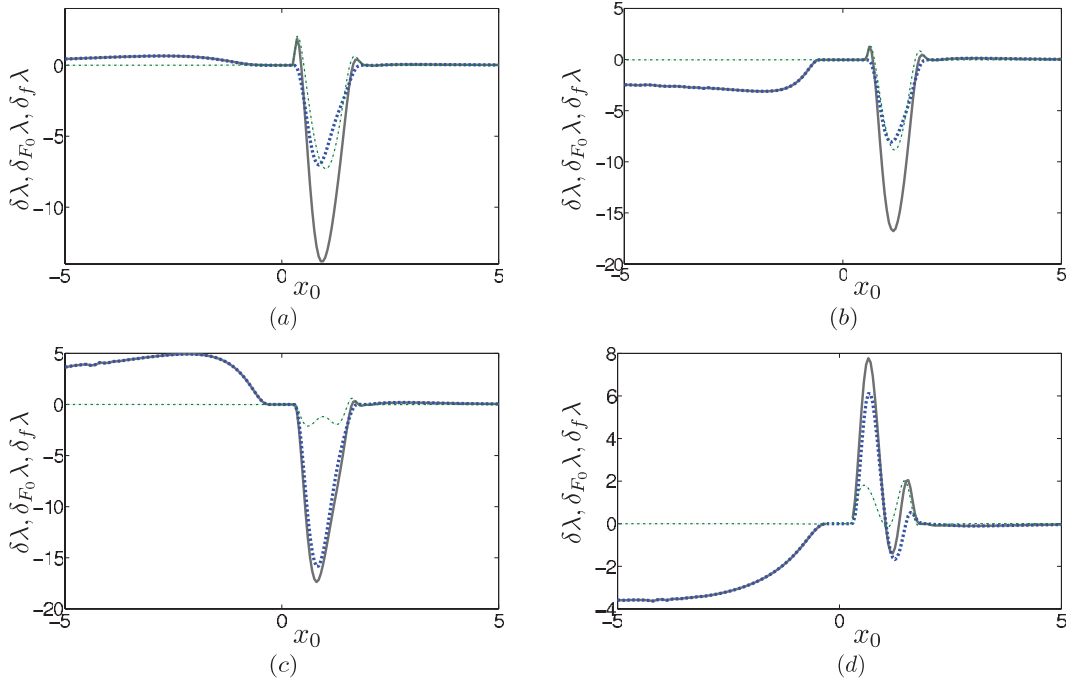


FIG. 15. Growth rate and frequency variations due to the forcing by a small body located on the axis of the base flow: (a) $\delta\lambda_{sta^-}/C$ for a bubble with $\chi = 2.5$ close to $Re = 155$; (b) same for a rigid sphere close to $Re = 212.9$; (c) $\mathcal{R}e(\delta\lambda_{osc^-})/C$; and (d) $\mathcal{I}m(\delta\lambda_{osc^-})/C$ for a bubble with $\chi = 2.5$ close to $Re = 215$. Blue/thick dashed line: base flow; green/thin dashed-dotted line: disturbance flow; gray/solid line: total flow. The bubble (resp. sphere) stands in the interval $x_0 = \pm 0.271 = (2\chi^{2/3})^{-1}$ (resp. $x_0 = \pm 0.5$).

to slightly destabilize that past the bubble. Note that in both cases, this effect occurs through the influence of the base flow only. We shall analyze its origin later.

Qualitatively similar features are noticed regarding the oscillating mode (Figure 15(c)), except that there is now no destabilizing zone right at the back of the bubble. The destabilizing effect of an upstream forcing is still present and is even stronger than that observed close to the first threshold. Finally, Figure 15(d) shows that the frequency of the oscillating mode is generally increased when the forcing is applied within the standing eddy, especially when it stands in its front part, say $x_0 \approx 0.4$. In contrast a forcing located within the central region $1.1 < x_0 < 1.4$ yields a slight decrease of the frequency. More spectacular is the strong decrease induced by a forcing placed at some distance upstream of the bubble. Note also that variations in the growth rate and frequency of the oscillating mode occur essentially through the effect of the base flow, except when the forcing is located very close to the separation line ($x_0 \approx 1.9$), a feature in line with our previous conclusions regarding the receptivity to a localized feedback (Figures 11(a) and 11(c)).

According to the above findings, the flow past an oblate bubble (hence probably its path) may be destabilized by introducing another small bubble or a small particle ahead of it, while this situation is found to stabilize the flow past a rigid sphere. Since this destabilization/stabilization process is driven by the base flow, Eq. (17a) suggests that examining the adjoint base velocity field around both types of body should provide some insight into the underlying mechanism. Indeed, Figure 16 shows that, although the two streamline patterns of \mathbf{U}_0^\dagger are qualitatively similar downstream of the body, they differ dramatically from each other ahead of it. In the case of a rigid sphere (Figure 16(b)), the streamlines that lie along the symmetry axis within the standing eddy circumvent the sphere as long as upstream advection is strong enough to overcome viscous effects in the boundary layer. However, the strength of these effects is such that separation eventually occurs near the equator of the sphere. Consequently, \mathbf{U}_0^\dagger is essentially parallel to \mathbf{U}_0 ahead of the sphere, i.e., no information coming from the wake reaches the upstream part of the flow and vice versa. In the case of a bubble, viscous effects in the boundary layer are weak (they essentially provide an $O(Re^{-1/2})$ -correction to the irrotational

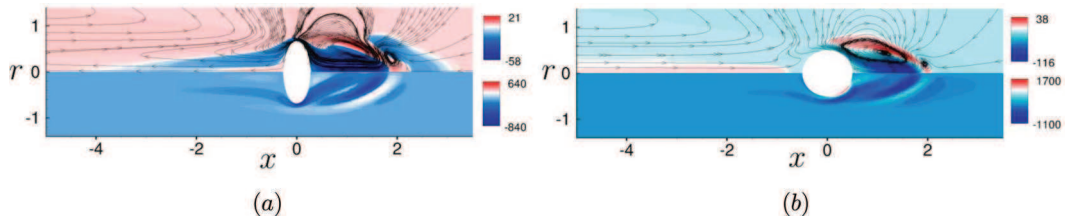


FIG. 16. Adjoint base flow around: (a) a bubble with $\chi = 2.5$ at $Re = 155$; (b) a rigid sphere at $Re = 212.9$. (Top) Velocity field and streamlines; (bottom) azimuthal vorticity. Note that, along the upstream part of the symmetry axis, the velocities are from right to left in (a) and from left to right in (b).

base flow⁴⁵). Therefore, no separation of the adjoint base flow occurs at the bubble surface and the downstream and upstream regions lying along the symmetry axis are connected by open streamlines that circumvent entirely the bubble (Figure 16(a)). This is how information is transferred between the near wake and the upstream region and why a small body standing at some upstream distance from the bubble along the symmetry axis is able to trigger wake instability whereas it can only stabilize the wake in the case the flow obeys a no-slip condition at the body surface.

VI. SUMMARY

We have carried out a systematic linear stability analysis of the flow past a fixed spheroidal bubble. In agreement with previous studies,^{9,10} two unstable global modes have been found to emerge from the steady axisymmetric state provided the bubble aspect ratio is large enough. When this condition is fulfilled, the flow is unstable within a finite range of Reynolds number only. The thresholds corresponding to the lower branch of the neutral curves agree very well with available DNS results,⁹ while those corresponding to the upper branch reveal significant differences presumably due to a slow time evolution of the base flow in the DNS. Whatever branch is considered, the first unstable mode, which is found to exist if $\chi \geq 2.2$, arises through a steady supercritical bifurcation and is made of two counter-rotating streamwise vortices. The second mode, which exists if $\chi \geq 2.41$, is time-dependent and arises through a Hopf bifurcation. Its structure reveals an alternation of positive and negative streamwise vortices. These modes keep qualitatively the same structure along both branches of the neutral curve. However, since streamwise advection increases with the Reynolds number, they are confined to the immediate vicinity of the axis of the base flow along the upper branch, which results in much more elongated vortical structures.

To identify the regions of the flow most sensitive to perturbations, we followed an adjoint-based approach. We successively examined the sensitivity of the wake to a localized feedback based on a linear force-velocity coupling, to base flow modifications and to an external local quadratic forcing modifying both the base flow and the global modes. In line with previous studies devoted to rigid bodies, we observed that the flow receptivity reaches its maximum in the core of the standing eddy and near the separation line for the stationary and oscillating modes, respectively. When the total flow is disturbed by a localized quadratic forcing which may be due to a second small bubble or to a small rigid particle, a stabilizing effect is obtained by applying the forcing in the core of the standing eddy. In contrast, a forcing applied near the separation line results in a slightly destabilizing effect on both global modes, while a more pronounced destabilization is obtained on the stationary mode if the forcing is applied right at the rear of the bubble. These observations are also similar to previous conclusions obtained with axisymmetric bodies at the surface of which the flow obeys a no-slip condition. Therefore, present findings reinforce the conclusions of Ref. 9 according to which the main mechanisms driving wake instability are qualitatively independent of the boundary condition at the body surface, the key quantity being the amount of vorticity generated at this surface and then injected in the flow. Nevertheless, significant levels of receptivity were noticed at various locations of the rear part of the bubble surface, especially just at the back of the equatorial plane, in contrast to the case of rigid bodies.

These findings were completed by examining the sensitivity of the flow to variations in the surface shear stress and normal velocity, respectively. The former component was found to be positive throughout the surface, indicating that a positive shear stress (directed toward the rear stagnation point of the bubble) always tends to destabilize the flow, especially if it applies near the separation line where the sensitivity was observed to reach its maximum. This general property of “surface sensitivity” which is specific to clean bubbles at the surface of which the flow obeys a shear-free condition may be directly connected to the well-known influence of surfactants on several aspects of bubble dynamics, such as the rise velocity and threshold of path instability.² The sensitivity to variations in the normal velocity at the bubble surface was found to be qualitatively similar to what is known about the effect of blowing and suction through the surface of rigid bodies. In particular, a local increase in the bubble radius was observed to be stabilizing over most of the surface area where the flow recirculates but is destabilizing anywhere else, especially in the region close to the equator of the bubble.

Another remarkable feature specific to bubbles that was identified here through the adjoint-based approach is the fact that a small body standing ahead of the bubble has a destabilizing effect on the two global modes, whereas it is stabilizing if the bubble is replaced by a solid body. We showed that this striking difference is due to the fact that the adjoint base velocity field separates along the surface in presence of a no-slip condition while it does not at the surface of a shear-free bubble, making the wake sensitive to the disturbance induced by the forcing in the latter case but not in the former.

The approach developed in this paper may be coupled with a realistic model of surfactant transport^{12,41,42} to assess the changes induced in the wake dynamics by the adsorption/desorption and surface transport mechanisms that drive the contamination of bubbles in many real fluids, especially water. Nevertheless the next step of this stream of research performed in our group will still consider clean bubbles. The main improvement with respect to the present paper will stand in the fact that the bubble will be allowed to rise freely under the action of buoyancy. In this new step, our goal will be to extend the present LSA to study how wake instability and kinematic degrees of freedom of the body combine to determine the dynamics of the fully coupled fluid-bubble system, following the approach we previously applied to two-dimensional plates and rods.¹⁴

ACKNOWLEDGMENTS

We warmly thank Flavio Giannetti for valuable comments and suggestions and Jérôme Mougel for his help with FreeFem++ and with the implementation of the shear-free boundary condition. This work was supported by the Agence Nationale de la Recherche under Grant No. ANR-09-BLAN-0132 OBLIC.

APPENDIX A: VARIATIONAL FORMULATION OF THE NAVIER-STOKES EQUATIONS WITH A SLIP CONDITION

Let us first rewrite Eq. (1c) in the form

$$\mathbf{T}(\mathbf{U}, P) \cdot \mathbf{n} = \Sigma(\mathbf{U}, P)\mathbf{n} \quad \text{on } \mathcal{S}_b, \quad (\text{A1})$$

where $\mathbf{T} = -P\mathbf{I} + 2Re^{-1}\mathbf{D}(\mathbf{U})$ is the stress tensor and $\Sigma(\mathbf{U}, P) = \mathbf{n} \cdot \mathbf{T} \cdot \mathbf{n}$ is the normal stress component, $\mathbf{D}(\mathbf{U}) = (\nabla\mathbf{U} + \nabla\mathbf{U}^T)/2$ denoting the strain-rate tensor.

To solve Eqs. (1) with a finite element method, a variational formulation of the problem is required. For this purpose, let us introduce the test functions $(\tilde{\mathbf{U}}, \tilde{P}, \tilde{\Sigma})$ for the velocity \mathbf{U} , pressure P and normal stress Σ , respectively. The reader is referred to Ref. 25 for the choice of the proper Hilbert spaces to which these test functions must belong in order to ensure suitable convergence properties. Let us only mention that, while $\tilde{\mathbf{U}}$ and \tilde{P} can, respectively, be chosen as P2 and P1 functions defined in the domain \mathcal{D} , $\tilde{\Sigma}$ can be taken as a P1 function defined on the bubble surface \mathcal{S}_b . The procedure described here was used for computing the base flow as well as the direct and adjoint modes.

Multiplying Eqs. (1a), (1b), and (1d) by the velocity, pressure, and stress test functions, respectively, and integrating by parts allows the dynamic condition (A1) to be naturally taken into account. Indeed, use of the divergence theorem yields

$$\langle -\nabla P + Re^{-1}\nabla^2\mathbf{U}, \tilde{\mathbf{U}} \rangle_{\mathcal{D}} = \langle P, \nabla \cdot \tilde{\mathbf{U}} \rangle_{\mathcal{D}} - 2Re^{-1} \langle \mathbf{D}(\mathbf{U}), \mathbf{D}(\tilde{\mathbf{U}}) \rangle_{\mathcal{D}} + \langle \mathbf{n} \cdot \mathbf{T}(\mathbf{U}, P), \tilde{\mathbf{U}} \rangle_{\mathcal{S}_b}, \quad (\text{A2a})$$

$$= \langle P, \nabla \cdot \tilde{\mathbf{U}} \rangle_{\mathcal{D}} - 2Re^{-1} \langle \mathbf{D}(\mathbf{U}), \mathbf{D}(\tilde{\mathbf{U}}) \rangle_{\mathcal{D}} + \langle \Sigma, \tilde{\mathbf{U}} \cdot \mathbf{n} \rangle_{\mathcal{S}_b}, \quad (\text{A2b})$$

where $\langle \cdot, \cdot \rangle$ denotes the inner products in the Hilbert spaces defined either in the volume \mathcal{D} or on the surface \mathcal{S}_b . Therefore, while the usual no-slip condition leads to a weak formulation with the velocity and pressure as unknowns, Eq. (A2) enables us to set up the problem with a slip condition on \mathcal{S}_b so as to find \mathbf{U} , P and Σ satisfying

$$\langle \partial_t \mathbf{U}, \tilde{\mathbf{U}} \rangle_{\mathcal{D}} + \langle \mathbf{U} \cdot \nabla \mathbf{U}, \tilde{\mathbf{U}} \rangle_{\mathcal{D}} = \langle P, \nabla \cdot \tilde{\mathbf{U}} \rangle_{\mathcal{D}} - 2Re^{-1} \langle \mathbf{D}(\mathbf{U}), \mathbf{D}(\tilde{\mathbf{U}}) \rangle_{\mathcal{D}} + \langle \Sigma, \tilde{\mathbf{U}} \cdot \mathbf{n} \rangle_{\mathcal{S}_b}, \quad (\text{A3a})$$

$$\langle \tilde{P}, \nabla \cdot \mathbf{U} \rangle_{\mathcal{D}} = 0, \quad (\text{A3b})$$

$$\langle \tilde{\Sigma}, \mathbf{U} \cdot \mathbf{n} \rangle_{\mathcal{S}_b} = 0. \quad (\text{A3c})$$

Now, expanding (\mathbf{U}, P, Σ) in the form $\mathbf{U} = \mathbf{U}_0 + \epsilon \mathbf{u}$, $P = P_0 + \epsilon p$, and $\Sigma = \Sigma_0 + \epsilon \sigma$, Eqs. (A3) can easily be made explicit for each mode. For that purpose, the unknown fields are first projected onto the space of the shape functions chosen to be identical to the test functions, so that

$$\mathbf{u} = \sum_j \mathbf{u}^j \cdot \tilde{\mathbf{U}}^j, \quad p = \sum_j p^j \tilde{P}^j, \quad \sigma = \sum_j \sigma^j \tilde{\Sigma}^j, \quad (\text{A4})$$

the summation being on the whole set of nodes. Hence the unknown vector becomes $\mathbf{q}^j = (\mathbf{u}^j, p^j, \sigma^j)^T$ with $\mathbf{u}^j = (u_r^j, u_\theta^j, u_x^j)^T$. Then, for a normal mode $\mathbf{q} = \hat{\mathbf{q}}(r, x)e^{\lambda t + im\theta}$, the generalized eigenvalue problem $\lambda \mathcal{B} \hat{\mathbf{q}} + \mathcal{A}_m \hat{\mathbf{q}} = \mathbf{0}$ resulting from Eqs. (A3) reads

$$\lambda \begin{pmatrix} \langle \tilde{\mathbf{U}}, \tilde{\mathbf{U}}^j \rangle_{\mathcal{D}} & 0 & 0 \\ 0 & 0 & 0 \\ 0 & 0 & 0 \end{pmatrix} \begin{pmatrix} \hat{\mathbf{u}}^j \\ \hat{p}^j \\ \hat{\sigma}^j \end{pmatrix} + \begin{pmatrix} \langle \tilde{\mathbf{U}}, \mathcal{C}_m(\tilde{\mathbf{U}}^j, \mathbf{U}_0) \rangle_{\mathcal{D}} + \frac{2}{Re} \langle \mathbf{D}(\tilde{\mathbf{U}}), \mathbf{D}_m(\tilde{\mathbf{U}}^j) \rangle_{\mathcal{D}} - \langle \nabla_m \cdot \tilde{\mathbf{U}}, \tilde{P}^j \rangle_{\mathcal{D}} - \langle \tilde{\mathbf{U}} \cdot \mathbf{n}, \tilde{\Sigma}^j \rangle_{\mathcal{S}_b} \\ \langle \tilde{P}, \nabla_m \cdot \tilde{\mathbf{U}}^j \rangle_{\mathcal{D}} & 0 & 0 \\ \langle \tilde{\Sigma}, \tilde{\mathbf{U}}^j \cdot \mathbf{n} \rangle_{\mathcal{S}_b} & 0 & 0 \end{pmatrix} \begin{pmatrix} \hat{\mathbf{u}}^j \\ \hat{p}^j \\ \hat{\sigma}^j \end{pmatrix} = \begin{pmatrix} \mathbf{0} \\ 0 \\ 0 \end{pmatrix}, \quad (\text{A5})$$

where $\mathbf{U}_0 = \sum_j \mathbf{U}_0^j \cdot \tilde{\mathbf{U}}^j$, $\nabla_m = (\partial_r, \frac{im}{r}, \partial_x)^T$, $\mathbf{D}_m(\tilde{\mathbf{U}}^j) = (\nabla_m \tilde{\mathbf{U}}^j + (\nabla_m \tilde{\mathbf{U}}^j)^T)/2$, and $\mathcal{C}_m(\tilde{\mathbf{U}}^j, \mathbf{U}_0) = \tilde{\mathbf{U}}^j \cdot \nabla \mathbf{U}_0 + \mathbf{U}_0 \cdot \nabla_m \tilde{\mathbf{U}}^j$ represent the linearized advection operator.

APPENDIX B: INFLUENCE OF GRID CHARACTERISTICS

We tested different grids by varying successively the position of the inlet (l_1), outlet (l_2), and top (h) of the domain with respect to the bubble, as well as the number N of triangles involved in the discretization. For a bubble with $\chi = 2.5$, the thresholds of the stationary and oscillatory modes along the lower branch of the marginal curve are $Re_{sta^-} \approx 155.4$ and $Re_{osc^-} \approx 215.6$, respectively. Table II reports the variations of the base drag coefficient C_D and the eigenvalues λ_{sta^-} and λ_{osc^-} slightly above these thresholds, i.e., for $Re = 160$ and $Re = 220$, respectively. It may be seen that all five grids provide very close values of the drag coefficient and frequency of the oscillatory mode. In particular, the drag coefficient is found to differ by less than 0.03% between the various grids, a good indication that the base flow is adequately resolved on all of them. The maximum differences on the growth rate of the stationary and oscillatory modes are about 1.4% and 5.7%,

TABLE II. Influence of grid characteristics on some quantities of interest slightly above the first two thresholds for a bubble with $\chi = 2.5$.

Grid number	l_2	l_1	h	N	$C_D(Re = 160)$	$\lambda_{sta^-}(Re=160)$	$C_D(Re = 220)$	$Re(\lambda_{osc^-})(Re=220)$	$Im(\lambda_{osc^-})(Re=220)$
1	89	23	33	19354	0.9263	9.85×10^{-3}	0.7335	4.15×10^{-3}	0.6984
2	114	23	33	19448	0.9263	9.83×10^{-3}	0.7335	4.13×10^{-3}	0.6984
3	89	44	33	19648	0.9261	9.82×10^{-3}	0.7334	4.15×10^{-3}	0.6983
4	89	23	55	21774	0.9263	9.86×10^{-3}	0.7335	4.14×10^{-3}	0.6984
5	89	23	33	26346	0.9264	9.96×10^{-3}	0.7336	4.38×10^{-3}	0.6984

respectively. We combined these results with a similar determination of the (negative) growth rates just below the thresholds, i.e., at $Re = 155$ and $Re = 215$, respectively, to locate the latter using a linear interpolation. It turned out that the maximum difference on Re_{sta^-} is about 0.04% (between Grids 3 and 5), while that on Re_{osc^-} is about 0.11% (between Grids 2 and 5). This comparison suggested that Grids 2 and 3 are slightly less accurate than the other three and we finally selected Grid 1 as the best compromise between accuracy and computational time. All results discussed in the paper were obtained with this grid.

APPENDIX C: DERIVATION OF THE SENSITIVITY OF EIGENVALUES TO AN EXTERNAL STEADY FORCING

The steady solutions of the Navier-Stokes equations associated with a given momentum forcing \mathcal{F}_0 in the bulk and given shear and normal velocity forcings τ_0 and W_0 at the body surface \mathcal{S}_b are governed by the non-homogeneous problem:

$$BF(\mathcal{Q}_0) = (\mathcal{F}_0, 0, 0)^T, \quad (\text{C1a})$$

$$W(\mathcal{Q}_0) = \mathbf{U}_0 \cdot \mathbf{n} = W_0, \quad (\text{C1b})$$

$$\tau(\mathcal{Q}_0)\mathbf{t} = (\mathbf{n} \cdot \mathbf{T}(\mathbf{U}_0, P_0) - \Sigma_0\mathbf{n}) = \tau_0\mathbf{t}, \quad (\text{C1c})$$

where $\mathbf{t} = \mathbf{n} \times \mathbf{e}_\theta$ is the local tangent unit vector to the bubble surface and the compact notation $BF(\mathcal{Q}_0)$ encompasses the momentum and mass conservation equations (2a) and (2b) plus the normal component of Eq. (2c) which defines Σ_0 as $\Sigma_0 = \mathbf{n} \cdot \mathbf{T}(\mathbf{U}_0, P_0) \cdot \mathbf{n} - P_0$ on \mathcal{S}_b . The base flow governed by Eqs. (2) therefore corresponds to $BF(\mathcal{Q}_0) = (\mathbf{0}, 0, 0)^T$, $W(\mathcal{Q}_0) = 0$, and $\tau(\mathcal{Q}_0) = 0$.

To determine the sensitivity of the eigenvalues to a small forcing increment $\delta\mathcal{G} \equiv \{\delta\mathcal{F}_0, 0, 0, \delta W_0, \delta\tau_0\}$, we define a functional \mathcal{L} which is such that $\delta\mathcal{L} = \delta\lambda$ when all constraints are satisfied. These constraints being the state equations (C1), this functional can be written as

$$\begin{aligned} \mathcal{L}(\lambda, \mathcal{Q}_0^\dagger, \mathcal{Q}_0, \hat{\mathbf{q}}, \hat{\mathbf{q}}^\dagger, \mathcal{G}) = & \lambda - \langle \hat{\mathbf{q}}^\dagger, (\mathcal{A}_1(\mathcal{Q}_0) + \lambda\mathcal{B})\hat{\mathbf{q}} \rangle - \langle \mathcal{Q}_0^\dagger, BF(\mathcal{Q}_0) - (\mathcal{F}_0, 0, 0)^T \rangle \\ & - \langle W_0^\dagger, W(\mathcal{Q}_0) - W_0 \rangle_{\mathcal{S}} - \langle \tau_0^\dagger, \tau(\mathcal{Q}_0) - \tau_0 \rangle_{\mathcal{S}}, \quad (\text{C2}) \end{aligned}$$

where W_0^\dagger and τ_0^\dagger denote the adjoint of the two forcings W_0 and τ_0 , respectively, and the adjoint base flow $\mathcal{Q}_0^\dagger = (\mathbf{U}_0^\dagger, P_0^\dagger, \Sigma_0^\dagger)$ may be seen as a Lagrange multiplier of the base flow \mathcal{Q}_0 given by the solution of the linear nonhomogeneous problem^{19,24} $\mathcal{A}_0^\dagger \mathcal{Q}_0^\dagger = \nabla_{\mathcal{Q}_0} \lambda$, supplemented with boundary conditions similar to Eqs. (8c) and (8d) at the bubble surface \mathcal{S}_b plus suitable conditions on the outer surface of \mathcal{D} ensuring that all boundary terms resulting from integration vanish.

The total variation $\delta\mathcal{L}$ can be computed by differentiating \mathcal{L} with respect to each of the variables $\lambda, \mathcal{Q}_0^\dagger, \mathcal{Q}_0, \hat{\mathbf{q}}, \hat{\mathbf{q}}^\dagger, \mathcal{G}$. The adjoint perturbations equations and the normalization condition of the adjoint mode lead to $(\partial_\lambda \mathcal{L})\delta\lambda = 0$ and $(\partial_{\hat{\mathbf{q}}} \mathcal{L})\delta\hat{\mathbf{q}} = 0$. Assuming that any modification of the base flow still satisfies Eq. (C1a) also yields $(\partial_{\mathcal{Q}_0^\dagger} \mathcal{L})\delta\mathcal{Q}_0^\dagger = 0$. Finally, we also have $(\partial_{\hat{\mathbf{q}}^\dagger} \mathcal{L})\delta\hat{\mathbf{q}}^\dagger = \langle \delta\hat{\mathbf{q}}^\dagger, (\mathcal{A}_1 + \lambda\mathcal{B})\hat{\mathbf{q}} \rangle = 0$, since $\hat{\mathbf{q}}$ always satisfies Eq. (5).

Therefore, we are left with

$$\delta\mathcal{L} = \frac{\partial\mathcal{L}}{\partial\mathcal{G}}\delta\mathcal{G} + \frac{\partial\mathcal{L}}{\partial\mathcal{Q}_0}\delta\mathcal{Q}_0. \quad (\text{C3})$$

The second term in the right-hand-side of Eq. (C3) may be expanded in the form

$$\frac{\partial\mathcal{L}}{\partial\mathcal{Q}_0}\delta\mathcal{Q}_0 = -\underbrace{\left\langle \hat{\mathbf{q}}^\dagger, \left[\frac{\partial}{\partial\mathcal{Q}_0}(\mathcal{A}_1\mathbf{q}) \right] \delta\mathcal{Q}_0 \right\rangle}_{(a)} - \underbrace{\left\langle \mathcal{Q}_0^\dagger, \mathcal{A}_0\delta\mathcal{Q}_0 \right\rangle}_{(b)} - \left\langle \mathbf{W}_0^\dagger, \delta\mathbf{W}_0 \right\rangle_{\mathcal{S}} - \left\langle \boldsymbol{\tau}_0^\dagger, \delta\boldsymbol{\tau}_0 \right\rangle_{\mathcal{S}}. \quad (\text{C4})$$

Term (a) in Eq. (C4) provides the sensitivity to base flow modifications in the form

$$(a) = -\left\langle \left[\frac{\partial}{\partial\mathcal{Q}_0}(\mathcal{A}_1\mathbf{q}) \right]^\dagger \cdot \hat{\mathbf{q}}^\dagger, \delta\mathcal{Q}_0 \right\rangle = \langle \nabla_{\mathcal{Q}_0}\lambda, \delta\mathcal{Q}_0 \rangle. \quad (\text{C5})$$

Then, integrating term (b) of Eq. (C4) by parts provides the governing equation for the adjoint base flow in the form:

$$(b) = -\left\langle \mathcal{A}_0^\dagger \mathcal{Q}_0^\dagger, \delta\mathcal{Q}_0 \right\rangle - \left\langle \boldsymbol{\Sigma}_0^\dagger, \delta\mathbf{W}_0 \right\rangle_{\mathcal{S}} + \left\langle \mathbf{U}_0^\dagger \cdot \mathbf{t}, \delta\boldsymbol{\tau}_0 \right\rangle_{\mathcal{S}}, \quad (\text{C6})$$

where use has been made of the boundary condition $\mathbf{U}_0^\dagger \cdot \mathbf{n} = 0$ at the bubble surface. In Eq. (C3), the variation with respect to the base flow then becomes

$$\begin{aligned} \frac{\partial\mathcal{L}}{\partial\mathcal{Q}_0}\delta\mathcal{Q}_0 &= \langle \nabla_{\mathcal{Q}_0}\lambda, \delta\mathcal{Q}_0 \rangle - \left\langle \mathcal{A}_0^\dagger \mathcal{Q}_0^\dagger, \delta\mathcal{Q}_0 \right\rangle - \left\langle \boldsymbol{\Sigma}_0^\dagger, \delta\mathbf{W}_0 \right\rangle_{\mathcal{S}} \\ &\quad + \left\langle \mathbf{U}_0^\dagger \cdot \mathbf{t}, \delta\boldsymbol{\tau}_0 \right\rangle_{\mathcal{S}} - \left\langle \mathbf{W}_0^\dagger, \delta\mathbf{W}_0 \right\rangle_{\mathcal{S}} - \left\langle \boldsymbol{\tau}_0^\dagger, \delta\boldsymbol{\tau}_0 \right\rangle_{\mathcal{S}}. \end{aligned} \quad (\text{C7})$$

Since the eigenvalue drift must vanish if \mathcal{G} does, Eq. (C3) must eventually reduce to the variation of \mathcal{L} with respect to \mathcal{G} , i.e., $(\partial_{\mathcal{Q}_0}\mathcal{L})\delta\mathcal{Q}_0$ must be zero. Canceling volume and surface terms separately in (C7) then yields the three conditions:

$$\mathcal{A}_0^\dagger \mathcal{Q}_0^\dagger = \nabla_{\mathcal{Q}_0}\lambda, \quad \mathbf{W}_0^\dagger = -\boldsymbol{\Sigma}_0^\dagger, \quad \text{and} \quad \boldsymbol{\tau}_0^\dagger = \mathbf{U}_0^\dagger \cdot \mathbf{t}. \quad (\text{C8})$$

Making use of (C2), the eigenvalue drift in Eq. (C3) is then found to reduce to

$$\delta\lambda = \frac{\partial\mathcal{L}}{\partial\mathcal{G}}\delta\mathcal{G} = \left\langle \mathcal{Q}_0^\dagger, (\delta\mathcal{F}_0, 0, 0)^T \right\rangle + \left\langle \mathbf{W}_0^\dagger, \delta\mathbf{W}_0 \right\rangle_{\mathcal{S}} + \left\langle \boldsymbol{\tau}_0^\dagger, \delta\boldsymbol{\tau}_0 \right\rangle_{\mathcal{S}}. \quad (\text{C9})$$

Finally, since the eigenvalue drift is defined as $\delta\lambda = \langle \nabla_{\mathcal{F}_0}\lambda, \delta\mathcal{F}_0 \rangle + \langle \nabla_{\mathbf{W}_0}\lambda, \delta\mathbf{W}_0 \rangle_{\mathcal{S}} + \langle \nabla_{\boldsymbol{\tau}_0}\lambda, \delta\boldsymbol{\tau}_0 \rangle_{\mathcal{S}}$, identifying this expression with Eq. (C9) allows us to conclude that the sensitivities with respect to \mathcal{F}_0 , \mathbf{W}_0 , and $\boldsymbol{\tau}_0$ read, respectively,

$$\nabla_{\mathcal{F}_0}\lambda = \mathcal{Q}_0^\dagger, \quad \nabla_{\mathbf{W}_0}\lambda = \mathbf{W}_0^\dagger = -\boldsymbol{\Sigma}_0^\dagger, \quad \text{and} \quad \nabla_{\boldsymbol{\tau}_0}\lambda = \boldsymbol{\tau}_0^\dagger = \mathbf{U}_0^\dagger \cdot \mathbf{t}. \quad (\text{C10})$$

Note that if the forcing were acting only on the variables $(\mathbf{U}_0, P_0, \boldsymbol{\Sigma}_0)$ defining \mathcal{Q}_0 and not on the surface quantities \mathbf{W}_0 and $\boldsymbol{\tau}_0$, Eq. (C9) would reduce to $\delta\lambda = \left\langle \mathcal{Q}_0^\dagger, \delta\mathcal{G} \right\rangle$ which may also be written as $\delta\lambda = \langle \nabla_{\mathcal{G}}\lambda, \delta\mathcal{G} \rangle$. Hence in that case one has directly

$$\nabla_{\mathcal{G}}\lambda = \mathcal{Q}_0^\dagger, \quad (\text{C11})$$

and the first of Eqs. (C8) may be rewritten in the form

$$\nabla_{\mathcal{Q}_0}\lambda = \mathcal{A}_0^\dagger \nabla_{\mathcal{G}}\lambda. \quad (\text{C12})$$

¹ A. Prosperetti, "Bubbles," *Phys. Fluids* **16**, 1852–1865 (2004).

² J. Magnaudet and I. Eames, "The motion of high-Reynolds-number bubbles in inhomogeneous flows," *Annu. Rev. Fluid Mech.* **32**, 659–708 (2000).

³ K. Ellingsen and F. Risso, "On the rise of an ellipsoidal bubble in water: Oscillatory paths and liquid-induced velocity," *J. Fluid Mech.* **440**, 235–268 (2001).

- ⁴ A. W. G. de Vries, A. Biesheuvel, and L. van Wijngaarden, "Notes on the path and wake of a gas bubble rising in pure water," *Int. J. Multiphase Flow* **28**, 1823–1835 (2002).
- ⁵ C. Veldhuis, A. Biesheuvel, and L. van Wijngaarden, "Shape oscillations on bubbles rising in clean and in tap water," *Phys. Fluids* **20**, 040705 (2008).
- ⁶ R. Zenit and J. Magnaudet, "Path instability of rising spheroidal air bubbles," *Phys. Fluids* **20**, 061702 (2008).
- ⁷ G. Mougouin and J. Magnaudet, "Path instability of a rising bubble," *Phys. Rev. Lett.* **88**, 014502 (2002).
- ⁸ G. Mougouin and J. Magnaudet, "Wake-induced forces and torques on a zigzagging/spiralling bubble," *J. Fluid Mech.* **567**, 185–194 (2006).
- ⁹ J. Magnaudet and G. Mougouin, "Wake instability of a fixed spheroidal bubble," *J. Fluid Mech.* **572**, 311–337 (2007).
- ¹⁰ B. Yang and A. Prosperetti, "Linear stability of the flow past a spheroidal bubble," *J. Fluid Mech.* **582**, 53–78 (2007).
- ¹¹ P. Ern, F. Risso, D. Fabre, and J. Magnaudet, "Wake-induced oscillatory paths of bodies freely rising or falling in fluids," *Annu. Rev. Fluid Mech.* **44**, 97–121 (2012).
- ¹² S. Takagi and Y. Matsumoto, "Surfactants effects on bubble motion and bubbly flows," *Annu. Rev. Fluid Mech.* **43**, 615–636 (2011).
- ¹³ S. Alben, "An implicit method for coupled flow-body dynamics," *J. Comput. Phys.* **227**, 4912–4933 (2008).
- ¹⁴ P. Assemat, D. Fabre, and J. Magnaudet, "The onset of unsteadiness of two-dimensional bodies falling or rising freely in a viscous fluid: A linear study," *J. Fluid Mech.* **690**, 173–202 (2012).
- ¹⁵ F. Auguste, J. Magnaudet, and D. Fabre, "Falling styles of disks," *J. Fluid Mech.* **719**, 388–405 (2013).
- ¹⁶ D. Sipp, O. Marquet, P. Meliga, and A. Barbagallo, "Dynamics and control of global instabilities in open flows: A linearized approach," *Appl. Mech. Rev.* **63**, 030801 (2010).
- ¹⁷ F. Giannetti and P. Luchini, "Structural sensitivity of the first instability of the cylinder wake," *J. Fluid Mech.* **581**, 167–197 (2007).
- ¹⁸ D. Sipp and A. Lebedev, "Global stability of base and mean flows: A general approach and its applications to cylinder and open cavity flows," *J. Fluid Mech.* **593**, 333–358 (2007).
- ¹⁹ O. Marquet, D. Sipp, and L. Jacquin, "Sensitivity analysis and passive control of cylinder flow," *J. Fluid Mech.* **615**, 221–252 (2008).
- ²⁰ J. O. Pralits, L. Brandt, and F. Giannetti, "Instability and sensitivity of the flow around a rotating cylinder," *J. Fluid Mech.* **650**, 513–536 (2010).
- ²¹ P. Meliga, J. M. Chomaz, and D. Sipp, "Unsteadiness in the wake of disks and spheres: Instabilities, receptivity and control using direct and adjoint global stability analyses," *J. Fluids Struct.* **25**, 601–616 (2009).
- ²² P. Meliga, J. M. Chomaz, and D. Sipp, "Global mode interaction and pattern selection in the wake of a disk: A weakly nonlinear expansion," *J. Fluid Mech.* **633**, 159–189 (2009).
- ²³ E. Sanmiguel-Rojas, A. Sevilla, C. Martínez-Bazán, and J. M. Chomaz, "Global mode analysis of axisymmetric bluff-body wakes: Stabilization by base bleed," *Phys. Fluids* **21**, 114102 (2009).
- ²⁴ P. Meliga, D. Sipp, and J. M. Chomaz, "Open-loop control of compressible afterbody flows using adjoint methods," *Phys. Fluids* **22**, 054109 (2010).
- ²⁵ R. Verfürth, "Finite element approximation of incompressible Navier-Stokes equations with slip boundary conditions II," *Numer. Math.* **59**, 615–635 (1991).
- ²⁶ L. Leal, "Vorticity transport and wake structure for bluff bodies at finite Reynolds number," *Phys. Fluids A* **1**, 124–131 (1989).
- ²⁷ A. Blanco and J. Magnaudet, "The structure of the axisymmetric high-Reynolds number flow around an ellipsoidal bubble of fixed shape," *Phys. Fluids* **7**, 1265–1274 (1995).
- ²⁸ D. Legendre, "On the relation between the drag and the vorticity produced on a clean bubble," *Phys. Fluids* **19**, 018102 (2007).
- ²⁹ D. Fabre, F. Auguste, and J. Magnaudet, "Bifurcations and symmetry breaking in the wake of axisymmetric bodies," *Phys. Fluids* **20**, 051702 (2008).
- ³⁰ P. C. Duineveld, "The rise velocity and shape of bubbles in pure water at high Reynolds number," *J. Fluid Mech.* **292**, 325–332 (1995).
- ³¹ J. C. Cano-Lozano, P. Bohorquez, and C. Martínez-Bazán, "Wake instability of a fixed axisymmetric bubble of realistic shape," *Int. J. Multiphase Flow* **51**, 11–21 (2013).
- ³² D. Fabre, J. Tchoufag, and J. Magnaudet, "The steady oblique path of buoyancy-driven disks and spheres," *J. Fluid Mech.* **707**, 24–36 (2012).
- ³³ R. Natarajan and A. Acrivos, "The instability of the steady flow past spheres and disks," *J. Fluid Mech.* **254**, 323–344 (1993).
- ³⁴ T. Johnson and V. Patel, "Flow past a sphere up to a Reynolds number of 300," *J. Fluid Mech.* **378**, 19–70 (1999).
- ³⁵ J. M. Chomaz, "Global instabilities in spatially developing flows: Non-normality and nonlinearity," *Annu. Rev. Fluid Mech.* **37**, 357–392 (2005).
- ³⁶ P. Schmid and D. Henningson, *Stability and Transition in Shear Flows* (Springer-Verlag, New York, 2001).
- ³⁷ P. Meliga, D. Sipp, and J. M. Chomaz, "Effect of compressibility on the global stability of axisymmetric wake flows," *J. Fluid Mech.* **660**, 499–526 (2010).
- ³⁸ P. Huerre and P. Monkewitz, "Local and global instabilities in spatially developing flows," *Annu. Rev. Fluid Mech.* **22**, 473–537 (1990).
- ³⁹ P. Bearman, "The effect of base bleed on the flow behind a two-dimensional model with a blunt trailing edge," *Aeronaut. Q.* **18**, 207–214 (1967).
- ⁴⁰ P. Bagchi, "Flow past a sphere with surface blowing and suction," *Trans. ASME-J. Fluids Eng.* **129**, 1547–1558 (2007).
- ⁴¹ B. Cuenot, J. Magnaudet, and B. Spennato, "The effects of slightly soluble surfactants on the flow around a spherical bubble," *J. Fluid Mech.* **339**, 25–53 (1997).

- ⁴²R. B. Fdhila and P. C. Duineveld, "The effect of surfactant on the rise of a spherical bubble at high Reynolds and Peclet numbers," *Phys. Fluids* **8**, 310–321 (1996).
- ⁴³A. Fani, S. Camarri, and M. V. Salvetti, "Stability analysis and control of the flow in a symmetric channel with a sudden expansion," *Phys. Fluids* **24**, 084102 (2012).
- ⁴⁴J. Magnaudet, M. Rivero, and J. Fabre, "Accelerated flows past a rigid sphere or a spherical bubble. Part 1. Steady straining flow," *J. Fluid Mech.* **284**, 97–135 (1995).
- ⁴⁵D. Moore, "The boundary layer on a spherical gas bubble," *J. Fluid Mech.* **16**, 161–176 (1963).